Novel Bio-inspired Aquatic Flow Sensors

Preston Albert Pinto

Thesis submitted to the Faculty of the Virginia Polytechnic Institute and State University
in partial fulfillment of the requirements for the degree of

Master of Science
In
Mechanical Engineering

Donald J. Leo, Chair
Stephen A. Sarles
Michael K. Philen
Pavlos Vlachos

June 18th, 2012
Blacksburg, Virginia

Keywords: artificial hair cell, flow sensor, lipid bilayer, regulated attachment method (RAM), artificial cell membrane, carbon nanotubes, carbon nanohorns

Novel Bio-inspired Aquatic Flow Sensors

Preston Albert Pinto

ABSTRACT

Inspired by the roles of hair cells in nature, this study aims to develop and characterize two new sets of novel flow sensors. One set of sensors developed and studied in this work are flow sensors fabricated using carbon nanomaterials. These sensors are made by embedding carbon nanotubes (CNT) and carbon nanohorns (CNH) into a polymeric substrate and then tested by flowing a conductive aqueous solution over the surface of the exposed CNT and CNH. In response, a flow-dependent voltage is generated. The surface coverage and the electrical relationship between the sensor and water is investigated and the voltage measurements of sensors with different levels of resistance were tested in varying fluid velocities. In response to these fluid velocities, the least resistive sensor showed small, but detectable changes in voltages, while higher resistance sensors showed less response. In addition, plasma treatment of the carbon nanomaterial/PDMS films were conducted in order to render the PDMS on the surface hydrophilic and in turn to pull more fluid towards the carbon material. This showed to improve the sensitivity of the flow sensors. This work also builds on previous research by investigating the flow dependent electrical response of a 'skin'-encapsulated artificial hair cell in an aqueous flow. An artificial cell membrane is housed in a flexible polyurethane substrate and serves as the transduction element for the artificial hair cell. Flow experiments are conducted by placing the bio-inspired sensor in a flow chamber and subjecting it to pulse-like flows. This study demonstrates that the encapsulated artificial hair cell flow sensor is capable of sensing changes in flow through a mechanoelectrical response and that its sensing capabilities may be altered by varying its surface morphology. Furthermore, the sensor's response and dynamics as a function of its surface morphology and structural properties are investigated through synchronized motion tracking of the hair with a laser vibrometer and current measurements across the artificial cell membrane.

Acknowledgements

Many people have contributed to the work presented in this thesis[1]. First and foremost, I would like to thank my advisor, Dr. Don Leo. His guidance, encouragement, support, and sense of humor have played an important role in not only this research project, but in my overall experience as a graduate student. Dr. Stephen Sarles (Andy) also deserves special recognition for his encouragement and friendship. His advice and the great example he set have significantly contributed to this work. Dr. Michael Philen has been very helpful and instrumental as well and deserves many thanks for his advice and recommendations. In addition, Dr. Pavlos Vlachos and Dr. Harry Dorn's group merit special thanks for their assistance and insights in this work.

I would like to recognize my many CIMSS colleagues for their friendships, technical guidance, and willingness to help. Beth Howell also deserves special thanks for the care and continuous support she has given to me. I would also like to acknowledge my friends for their encouragement and for the countless bored hours spent together. Finally, I am grateful to my parents and my sisters for all the love, much-needed discipline, and inspiration they have provided me with throughout the years.

PRESTON PINTO

Virginia Polytechnic Institute and State University

18th June 2012

[1] The author would like to acknowledge the Office of Naval Research for the financial support (N000140810654).

Table of Contents

List of Figures

List of Tables

Chapter 1

Introduction and Literature Review

The science of biomimicry has long allowed researchers and scientists to create the technologies of tomorrow by learning from nature's methods and solutions. Learning from nature can transform the way we fabricate materials, grow food, harvest energy, store and utilize information, and cure ourselves [1]. From the aerodynamic design of airplanes to the adhesion properties of Velcro, nature has in fact inspired our technologies and solutions. The design of the Japanese Shinkansen bullet train is one instance of the number of solutions nature has provided to our world. One of the problems associated with the high-speed train during its development was the occurrence of low-level sonic booms during its exit of tunnels. The sudden change in air resistance experienced by the train as it left a tunnel, caused this sonic boom. In order to solve this issue, the design team looked to the specially designed beak of the kingfisher bird. The kingfisher is able to catch its prey by diving from the air into the water with minimal energy loss and without splashing the water. The wedge shape of its beak and rounded head allows it to make this smooth and effortless entry into its new medium. As a result, by re-designing the train's nose to mimic the wedge shape of the kingfisher, the design team was able to eliminate the sonic booms [2]. Examples such as this shows how biomimicry has and will continue to provide us with innovative and sustainable solutions.

1.1 Literature Review

Apart from mimicking the structures of living organisms and natural materials, researchers have also been interested in mimicking the functions, specifically the sensing capabilities, of living organisms. Starting in the 1970s and over the past few

years, there have been many designs and developments of the cochlear implant, an artificial hearing device that is capable of sending sound information to the auditory centers of the brain via electrical simulation of the auditory nerve [3]. These designs include a low powered radio receiver chip capable of functioning like the human ear by deciphering sound through mechanical-to-electrical mapping and a piezoelectric acoustic sensor, which is capable of both acoustic/electric conversion and frequency selectivity [4, 5]. Aside from artificial hearing, researchers at Stanford have recently developed a skin-like pressure and strain sensor using carbon nanotubes. This artificial skin is based on transparent elastic films that can be wrapped around and integrated with a variety of non-planar and biological structures and surfaces [6]. These breakthroughs in artificial sensing will take technological developments to new levels of sophistication, because through the basic capability of sensation, we will be able to better detect, understand, and adapt to our environments.

1.1.1 Roles of hair-cells in Nature

Sensory receptors are found throughout nature and give animals the ability to sense stimuli in the world around them. These receptors are specialized cells that detect a variety of stimuli and transmit it to sensory nerves and the brain. The functions of sensory receptors include photoreception (sight), mechanoreception (touch, hearing, and balance), and chemoreception (smell and taste) [7]. For instance, our ability to maintain balance and detect sound is highly dependent on the hair cells found in our inner ear. These mechanosensory cells carry out the conversion of mechanical stimuli caused by sound waves and head movements into electrical signals, which are then processed by the nervous system [8]. The sensory receptors of all animal species have evolved in order to make animals better suited to their environments. For instance, while a bat and eagle both depend on specialized sensory receptors to find their prey, the receptors used by each animal are very different. A bat uses its ears to locate prey at night while an eagle uses its eyes from extreme heights to prevent detection from and

to spot prey [7]. The sensory receptors of animals found in the ocean are another great example of this specialized evolution. Specifically, inhabitants found in the deep ocean are capable of feeling, hearing, smelling, and tasting stimuli around them through a variety of hair-like receptors. Through pore-bearing chemoreceptors, some oceanic organisms are able to taste and smell chemical cues in the water in order to perform behaviors such as feeding, predator deterrence, and sex pheromones detection [9]. For example, research has shown that copepods can effectively differentiate and selectively feed on various species of phytoplankton by using chemoreceptors to perceive them from a distance and then changing the flow fields around their bodies in order to capture them [10, 11]. Apart from smelling and tasting chemicals around them, organisms in the ocean are also able to hear and feel stimuli around them by sensing a variety of hydrodynamic disturbances in their environment [9]. Similarly, harbor seals are able to detect small movements in water using their whiskers in order to locate prey and be warned of predators. This hydrodynamic sensory system has also been shown to help blind, but healthy seals successfully orient themselves and hunt without vision [12, 13]. The inertial, lateral, and hearing systems that fish have developed are yet another example of an intricate arrangement of hydrodynamic receptors. These complex systems are based on a single type of receptor cell known as the hair cell [9]. These hair cells help make up a crucial sensory systems of fish, the lateral line, which allows a fish to sense water movements around its body [14]. The lateral line consists of groups of receptors, called neuromasts, which are arranged along the horizontal mid-plane of the fish. Flow-induced deflections of hair cells within each neuromast trigger a neural response, which allows the fish to sense changes in the flow fields around its body and if needed, to exploit vortices in order to decrease muscle activity [15, 16].

1.1.2 Artificial Flow Sensors

Over the years, there have been many developments in mimicking a variety of hair cells by designing and fabricating sensors that use a variety of acoustic, thermal, pressure, and electromechanical sensing principles to sense changes in flow. For instance, using

MEMS (microelectromechanical system) techniques, cantilever beam-designed hairs that use a strain gauge to convert mechanical deformation to an electrical signal have been developed by Liu, et al [17]. Liu and his team were able to demonstrate the flow localization capability of the artificial lateral line [18]. Using a different sensing method, Chen, *et. al* have been able to mimic the lateral line's hydrodynamic imaging function by creating artificial hairs using elevated hot-wire elements to detect changes in flow [19-21]. Specifically, these thermal flow sensors work by using thermal anemometry, which correlates the convective heat transfer from the hot wire to the flow rate. As a result of this property, they can also be utilized as temperature sensors. Although the majority of these hot-wire sensors are made through macroscopic machining methods, micromachined hot-wire anemometers have also been fabricated [17, 22-25]. Various microfabrication techniques such as transfer molding [26], plastic deformation magnetic assembly [27], wire bonding [28], and photolithographic patterning [29] have been used to fabricated artificial hair cells. Sensing methods such as capacitive sensing and piezoresisitive sensing, and materials such as silicon, polyimide, and polyurethane have been used to build these synthetic hair cells [28, 29]. The combination of these materials and methods has led to the development of flow sensors that have a velocity and angular sensitivity under steady-state and oscillatory water flow conditions[30]. Most recently though, in order to better mimic hair cells, specifically the neuromasts found on fish, researchers have developed hydrogel-encapsulated piezoresistive hairs, which have the capability to reduce background noise and improve flow detection [31, 32].

1.2 Motivation and Plan for Developing Novel Aquatic Flow Sensors

For many years now, engineers have studied the locomotion of animals in order to build more effective and more efficient vehicles. As introduced in the previous section, one such topic that has been of particular interest is fish kinematics, because of the remarkable ability fish have to maneuver in tight areas, hover efficiently, quickly brake,

and perform high acceleration propulsion without sacrificing stability [33]. For example, Lauder's research group has investigated the function of fish fins during vertical and horizontal maneuvering in order to better understand the hydrodynamic role of fins [34, 35]. Specifically, they have researched the kinematics and propulsive properties of fish pectoral, dorsal, and caudal fins in order to help in the development of the next generation of aquatic robots [36]. Building on this information, Zhang, *et al.* [14] recently created a bio-inspired prototype fish, capable of an undulatory swimming using a flexible matrix composite (FMC) muscle technology developed by Philen, *et al* [37]. In conjunction with understanding and mimicking the swimming behavior of fish, researchers such as Lauder and Tangorra have been working to close the loop between the sensing mechanisms and control strategies that fish employ for regulating their motions [14]. Although the sensory receptors found on oceanic organisms are a great display of the variety of receptors present in nature, the ocean is not the only environment with sensory receptors in a fluid environment. For example, the fluid-filled structure of the cochlea, found in the inner ear, contain hair cells that allow for the interpretation of sound by the brain. These hair cells extend from the basilar membrane, a structural element that lines the inner wall of the cochlea and runs its entire length. The membrane is narrow and stiffer in structure at the base of the cochlea, but increases in width and becomes more flexible at the top. This variation in its width and stiffness allows the basilar membrane to pick up a range of sound frequencies. Since the membrane also acts as the base for the sensory cells, the vibrations along the membrane are transferred to these hair cells. Therefore, these hair cells are responsible for translating the fluid vibration of sound into electrical impulses that are carried to the brain through sensory nerves [7, 38]. As part of this larger effort to understand how sensing and neural feedback in a fluid environment regulate the behavior of animals, our group is developing novel aquatic flow sensors that are inspired by the sensory receptors found in not only the ocean, but throughout nature.

With a similar function to the lateral line and the various flow-sensing mechanoreceptors found in the ocean, recent research has shown that carbon nanotubes (CNT) arranged

on the surface of a supporting substrate produce a voltage proportional to the flow rate of water flowing across the exposed CNT surface. In addition to CNT structures, other carbonaceous materials, such as carbon peapods [39], graphene [40] and single walled carbon nanohorns (SWCNH) [41], exist that may shed light on the transduction mechanism that enables the flow of water to generate an electrical potential. In addition, by varying the basic structure of the carbon material, higher sensitivity flow sensors may be developed. Carbon nanohorns are closed tubules with conical ends, typically 2-10 nm in diameter and 10-70 nm long and have several advantages over carbon nanotubes including their ease of fabrication and higher purity [41]. Furthermore, the chemical composition of carbon nanohorns can be tailored to include other chemical elements. In particular, Zhang, *et al*. demonstrated that SWNHs can be used as MRI and X-ray contrast agents [41] by encapsulating trimetallic nitride template endohedral metallofullerenes (TNT-EMFs) inside SWNHs. This multifunctional ability of SWNHs opens up the possibility of creating artificial neuromasts with the ability to sense flow fields and image the CNHs on the surface. Therefore, motivated by the transduction mechanisms of single walled carbon nanotubes (SWCNT) and SWCNH, this work presents our development and characterization of two types of flow sensors that use carbonaceous materials supported on a polymeric substrate

The commonality of current flow sensor developments is they all use the properties of a synthetic material to produce a response than can be correlated to the bending and sensing capability of a hair. Over the past few years, our group has developed membrane-based biomolecular materials as a new class of smart materials [42-44]. These biomolecular materials use an artificial cell membrane as the transduction element and the selective barrier, which is a function of membranes in actual cells. The main components of a cell membrane as shown in Figure 1.1 are the phospholipid molecules, which are organized into a lipid bilayer [45]. The lipid molecules in this bilayer are composed of a hydrophilic head group and a hydrophobic tail group [46-48]. These properties of the phospholipid molecules drive the ordered formation of the lipid bilayer into a fluid-like structure [49] that allows it to work as a selective barrier and as a

housing for proteins . The existence of proteins in the bilayer allows the cell to carry out a variety of tasks from the maintenance of ion concentration to the sensing of an external environment [50, 51].

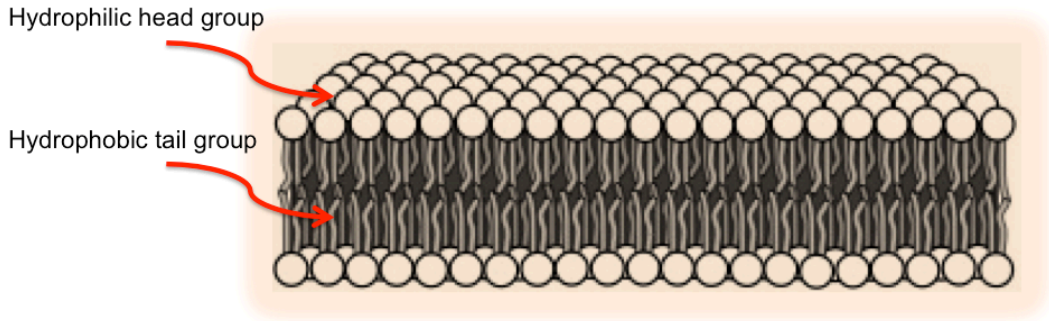

Figure 1.1. The structure of the cell membrane is composed of a bilayer arrangement of phospholipid molecules, which are composed of a hydrophilic head group and a hydrophobic tail group [52].

The smart materials created by our group feature artificial lipid bilayers contained within durable synthetic substrates. Specifically, these substrates contain a two-compartment network with a single lipid bilayer interface. Each compartment contains a hydrophilic lipid-encased aqueous phase and an exterior region containing a hydrophobic oil phase. The lipid-encased aqueous phases self- assemble at the hydrophilic–hydrophobic interface and as a result form an artificial cell membrane as shown below in Figure 1.2 [53].

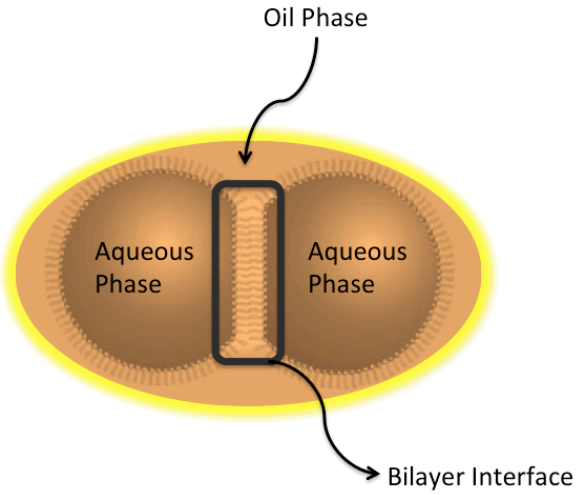

Figure 1.2. The artificial cell membrane is formed when the lipid-encased aqueous phases self-assemble at the hydrophilic-hydrophobic interface .

In our group's previous work, hair cell inspired gel-supported, artificial lipid bilayers were encased in flexible substrates and used as airflow sensors [54]. The sensor presented in this work uses an artificial cell membrane as a mechanoelectric transduction element, but unlike the air flow sensor presented in our earlier work, it is developed to endure and sense in aquatic environments, much like the lateral line found on the fish or the basilar membrane found in the cochlea of the human ear. Transitioning from synthetic materials to biomolecular materials will result in sensors that better mimic the structure and sensing capabilities of hair cells in nature. Specifically, our goal in using an artificial cell membrane-based sensor is to build receptors that can effectively sense flow and vibration in an aquatic environment as well as other stimuli such as light and chemicals. Moreover, by using a biomolecular building block, we pave the way for developing artificial receptors that can communicate, actuate, and convert energy, much like the sensing and neural feedback regulation used by sensory receptors throughout nature.

Chapter 2

Flow Sensors Fabricated from Carbon Nanomaterials

The use of carbon nanotubes for flow sensing was first demonstrated by Gosh, *et al*. [55] and Cao, *et al.* [56] by flowing a conductive liquid over an exposed single walled carbon nanotubes (SWCNT) surface in order to generate a flow-dependent voltage. These experiments demonstrated that the voltage generated depends on flow rate, the ionic conductivity of the liquid, and the amount of SWCNT surface coverage [55-58]. However as a result of varying fabrication methods, the voltage measured by the two groups varied significantly. Gosh, *et al*. fabricated the flow sensor by packing bundles of SWCNT between two metal electrodes and then holding them in place with two insulating substrates [57]. Current and voltage measurements were taken by taking electrical leads out from the metal electrodes. Since the bundles were only tightly packed onto the substrate surface and not held down, the flow of an aqueous solution of 0.01 M KCl slowly washed them away. At a flow speed of 0.4 mm/s, the flow-induced voltage was about 10 μV. Cao, *et al*. solved the problem of SWCNT bundles being washed away by using a different fabrication method. Instead of depositing SWCNTs onto a substrate, a SWCNT network/polydimethylsiloxane (PDMS) composite thin film was fabricated [56]. Embedding the SWCNTs into cured PDMS created the composite thin film. This approach prevented the nanotubes bundles from being washed away in the flow and therefore resulted in a more stable sensor [58]. When NaCl solution with a 5% concentration was flowed over the sample at 0.4 mm/s, a voltage of 19.01 mV was generated.

In our work we develop an initial series of samples that use two types of carbonaceous materials (SWCNT and SWCNH) supported on a polymeric substrate. While our fabrication methods are based on those used in previous studies, we believe that

published work to date has not been complete in the description of the necessary fabrication steps and sensor characterization. Therefore in this document, we present a preliminary study of the surface structure and sensing response of sensors constructed using the procedures based on methods developed by Cao, *et al.* Sensing measurements are performed in salt water (5% NaCl) and electrical impedance spectroscopy (EIS) is also used to correlate the equivalent electrical circuit of each sensor to the fabrication procedure and surface coverage.

2.1 Materials and Methods

2.1.1 Composite Film Fabrication

A Kimble & Chase vacuum microfiltration assembly containing a 47 mm fritted glass support is placed on a vacuum flask. A 47 mm Sterlitech polycarbonate membrane with a pore size of 0.2μm is rinsed with ethanol (Sigma Aldrich) and placed on top of the glass frit. A funnel is then placed on top of the fritter glass and clamped into place. A solution of SWCNT (or SWCNH) in ethanol is poured into the funnel and the ethanol is allowed to drain through the filter completely. Meanwhile, 10mL of PDMS prepolymer (Sylgard184, Dow Corning) is mixed with 1mL of the curing agent and allowed to rest in order to remove air bubbles. The membrane is then removed from the frit and placed into a glass dish where it is taped down to the glass to prevent PDMS from leaking underneath the porous membrane. The mixed PDMS is slowly poured over the membrane in the glass dish, and the dish is tapped gently on a surface to remove any newly formed bubbles. Once free of bubbles, the PDMS is allowed to cure at room temperature over night. The PDMS with embedded SWCNT/CNH is then removed from the dish, leaving the membrane taped to the glass dish. This procedure produces a relatively thick piece of PDMS (~1-3mm) coated with a surface layer of SWCNT/CNH and PDMS. Initially, in this study, four different SWCNT/PDMS films and two different SWCNH/PDMS films are fabricated and characterized.

2.1.2 Sensor Fabrication

The flow sensors are formed by first cutting the SWCNT/PDMS and SWCNH/PDMS films into 25 mm x 7 mm strips and then depositing conductive electrode pads (spaced 10 mm apart) on the surfaces of each sensor. The conductive electrode pads are made from Chemtronics conductive silver epoxy. In order to create electric leads, copper wire (36 AWG, Dabum Electronics and Cable) is embedded in the electrode pads and then placed on a hot plate to quickly bond the pads, leads, and film together.

2.1.3 Electrical Impedance Spectroscopy

The electrical impedance of the electrode SWCNT/PDMS sensors was performed in both air and in salt water using an Autolab PGSTAT12 potentiostat (Eco Chemie) and FRA software. For these measurements, a sinusoidal voltage of 100mV (RMS) was applied to the samples across the frequency range from 100kHz to 0.1Hz.

2.1.4 Flow Chamber Description and Measurements

The sensors are tested in a 43.18 cm long flow chamber, made from rectangular, acrylic tubing (22mm x 22mm). An impeller pump (DDC-3.2 TPMP., Laing) controlled by the applied voltage to the pump is used to provide continuous flow through the flow circuit. The fluid was delivered from the pump into the chamber through silicone tubing with an inner diameter of 6.4 mm. In order to reduce the effects of turbulence caused by the expansion of the flow into the flow chamber, the sample was placed approximately 50 mm from the entrance of the rectangular tubing. A rectangular window was made in the top of the tubing at this location in order to allow for easy placement of a sensor in the flow chamber. Flow measurements and EIS measurements in water (with no flow) were performed using 5% (wt./vol) sodium chloride (NaCl, Sigma Aldrich) as the aqueous phase in the flow circuit. A schematic of the flow chamber setup is shown in Figure 2.1.

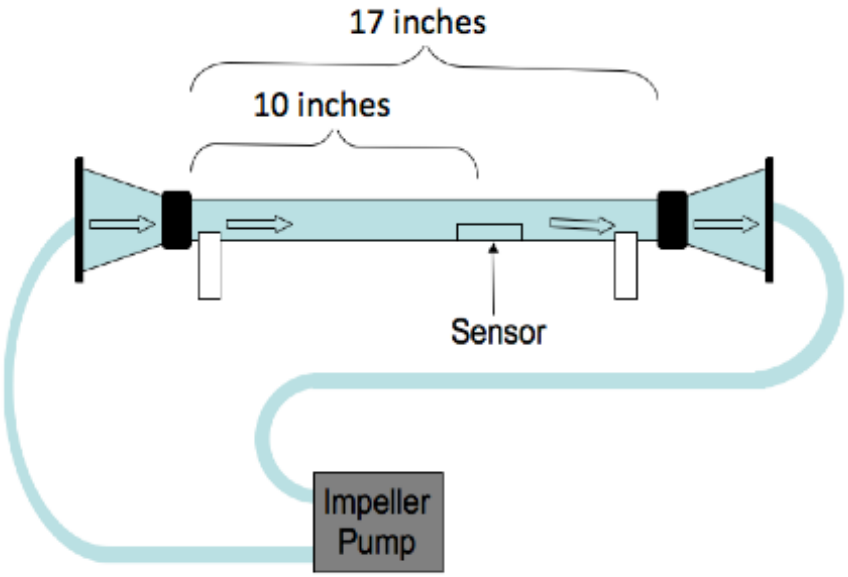

Figure 2.1. Flow chamber setup uses an impeller pump to deliver fluid through the acrylic chamber

Prior to flow characterization of the fabricated sensors, the flow velocity produced by the impeller pump was measured for varying voltage levels used to run the pump. A differential pressure sensor (1-Inch-D-MV, All Sensors, Corp) is used to measure the total pressure of flow water in the chamber. The sensor, which has a total range of 0-249Pa and a dynamic response time of <100μs is powered directly with ±8V. The output voltage from the sensor is sampled (256Hz) using a SigLab Model 20-42 (DSP Technologies). The total pressure is recorded by connecting an extension tube (2mm I.D.) to one of the pressure ports on the sensor and extending it into the flow chamber such that the tip of the extension tube is positioned parallel to the oncoming flow at the midplane of the chamber. Pressure measurements were collected for 20s at each pump voltage setting. Average flow velocity values are obtained by subtracting the hydrostatic pressure component (dc offset) measured at zero flow in order to compute dynamic pressure, as given below by:

$$P_D = \frac{1}{2}\rho V^2 \quad (2.1)$$

where, ρ is the density of water (kg/m^3) and V (m/s) is the flow velocity of water in the chamber. Table 2.1 lists the average measured flow velocities and volumetric flow rates for four different voltages applied to the impeller pump.

Table 2.1. Measured Flow Velocities and Volumetric Flowrates

Pump Voltage (V)	Flow Velocity (mm/s)	Volumetric Flow Rate (L/min)
6	96.1	2.56
8	131	3.49
10	143	3.82
12	191	5.09

Flow sensing measurements were performed for each sensor separately with the sensor positioned on the bottom inner surface of the rectangular chamber and oriented parallel to the flow as shown in Figure 2.2.

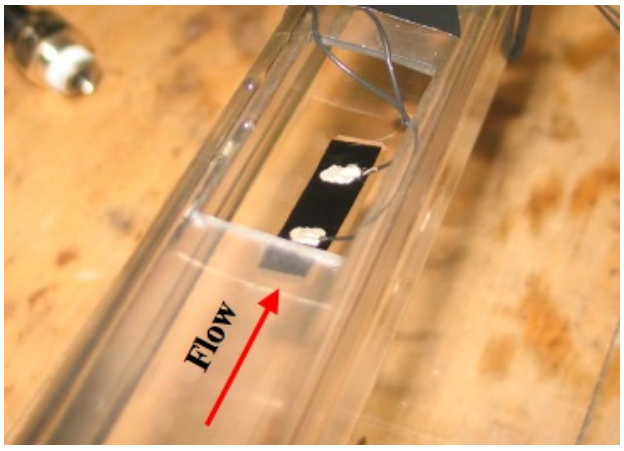

Figure 2.2. SWCNT/PDMS and SWCNH/PDMS sensors are placed at the bottom surface of the chamber and oriented parallel to the flow

For each sensor, the flow velocity of the water is varied by either altering the applied voltage to the impeller or by closing a valve connected in line between the rectangular chamber and the pump. Measurements of voltage and current in the sensor are obtained at a sampling rate of 10Hz using the Autolab PGSTAT12 and GPES software.

2.2 Results and Discussion

2.2.1 Surface Coverage Characterization

Using the fabrication procedure described in Section 2, two sets of material samples were created for building electrode-containing flow sensors: SWCNT/PDMS samples and SWCNH/PDMS samples. Images of both sets are shown in Figure 2.3. On a macroscopic level, both classes of materials feature a black surface coating of carbonaceous material. In the case of samples coated with CNTs, the surface has a matte, non-glossy finish, while those made with CNH appear glossier. Some surface texture is seen at this length scale and is attributed to wrinkles that develop in the filter membrane during the PDMS curing step.

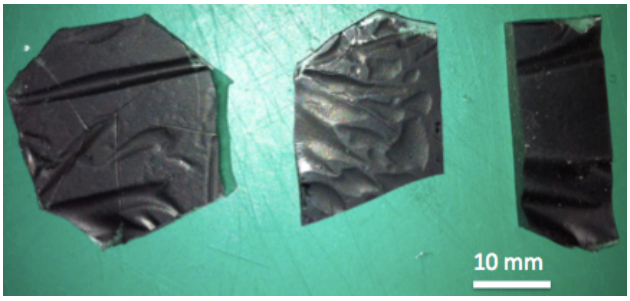

(a)

(b)

Figure 2.3. (a) CNH/PDMS samples and (b) electroded CNT/PDMS flow sensors. Note: the distance between the conductive electrodes is approximately 10 mm.

In an effort to characterize the morphology and surface topology of both classes of surface coatings, our team has used scanning electron microscopy (SEM), x-ray photoelectron spectroscopy (XPS), and even atomic form microscopy (AFM) to study the nanoscale surface features of these materials. Two SEM images of a sample of carbon nanohorn-coated PDMS is shown in Figure 2.4. These images indicate a drastic transition from the relatively featureless bulk PDMS to the textured composite surface film of CNH and PDMS (Figure 2.4a). The apparent thickness of this layer is on the order of 10μm, and the topology shows a highly wrinkled surface texture. At higher magnification (Figure 2.4b), some sub-micron surface features are detectable, however, these are likely artifacts of the molding procedure, since aggregates of SWCNH have dimensions of only 10-70 nm [41]. As a result, these images alone do not indicate the relative percentage of CNH versus PDMS.

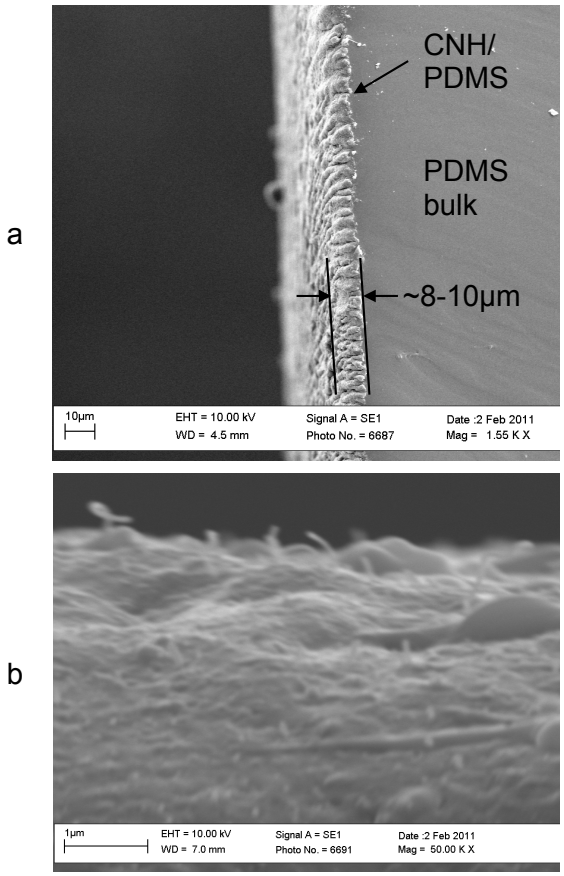

Figure 2.4. Images of the composite surface coating of single-walled carbon nanohorns and polydimethylsiloxane (SWCNH/PDMS) are obtained through scanning electron microscopy

In contrast, carbon nanotube-based composites, due to larger dimensions of CNT structures, may provide a more uniform surface coating of carbonaceous material, with less inter-dispersion of PDMS. In fact, Cao, *et al.* demonstrated that with SEM imaging that coating PDMS materials with 30μm long CNT results in the formation of highly-dense CNT surface coatings, where individual CNTs extend freely approximately 1-5μm from the PDMS base [56, 58].

As a second method to quantify the surface coverage of both the CNT-coated and CNH-coated samples, the electrical resistance was measured across the surface of each composite film using a standard two-probe multi-meter (Fluke 87). Measurements were

made with the multi-meter probes (approximately 10mm apart) placed on the surface of the samples. All CNH/PDMS samples had electrical resistances greater than 10kΩ, with several having resistance values greater than 100kΩ. In contrast, the CNT/PDMS samples had much lower electric resistances. Two of the samples had resistances on the order of 200-300Ω and two had resistances of several kΩ. Considering that the electrical resistance provides a measure of the conductivity across the surface and that PDMS is an insulating material, these measurements demonstrate that the CNT/PDMS composite films contain less PDMS at the outer surface of the sample. In contrast, the higher electrical resistances of the CNH/PDMS samples, despite their similar visual appearances, indicate that the outer surface contains a larger amount of PDMS. As a result, only the CNT/PDMS composite films were characterized in initial tests, since the lower resistance suggests these films will have more interaction between the CNT and the flowing water. Cao, *et al*. verified this same trend in their measurements of CNT based flow sensors, where they showed that a lower surface conductivity (i.e. higher resistance) results in less voltage output of the sensor. Therefore, in the following sections, our initial study of sensor performance examines the sensing capability for the four SWCNT/PDMS sensors [56, 58].

2.2.2 Electrical Impedance Spectroscopy

EIS measurements of the four SWCNT/PDMS sensors with attached electrodes were performed in both air and water in order to characterize the impedance of the sensor surface by itself (air) as well as understand the electrical interaction between the sensor and salt water during flow tests. An example EIS measurement for one SWCNT sensor in air and in water is shown in Figure 2.5. This plot shows both the magnitude of the impedance and the phase angle of the impedance versus frequency. For the measurement in air, the conductive SWCNT displays a constant magnitude of impedance and phase angle of 316Ω and 0°, respectively. This behavior suggests that the composite film of SWCNT/PDMS behaves like a pure resistor. When the same

sample is submerged in salt water (5%), the electrical impedance response becomes more capacitive due to the addition of a parallel conduction pathway through the electrolyte. The capacitive nature of the response is evident by the presence of negative phase measurements and a decreasing magnitude of impedance as the frequency increases.

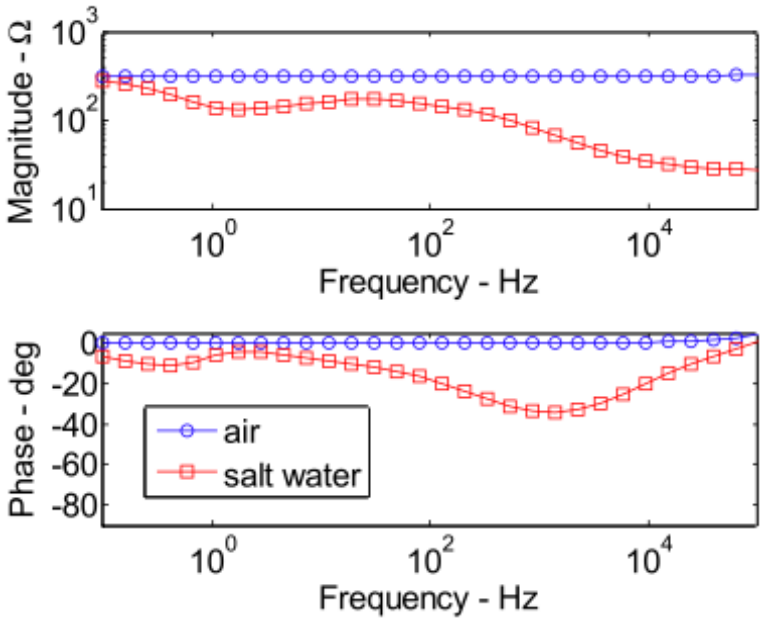

Figure 2.5. The magnitude (top) and phase angle (bottom) of the electrical impedance versus frequency for a single SWCNT/PDMS flow sensor in both air (blue circles) and water (red squares).

The EIS data in Figure 2.5 also shows that the collective impedance of the electrolyte and CNT surface is lower in salt water than of just the CNT surface in air. This result suggests that the salt water is more conductive across the same frequency range than the CNT surface. Despite several demonstrations of voltage produced by CNT-based flow sensors [55-57] the electrical impedance characteristics of these materials (or of the electroded sensors) has not been performed prior to this work.

EIS measurements of the other three SWCNT/PDMS sensors were performed in the same manner and the results followed the same trend. In each case, the sensor surface in air exhibits purely resistive behavior, while the collective measurement in water demonstrated the addition of a less-resistive, parallel conduction pathway. In summary, the measured values of electrical resistance for the four SWCNT/PDMS sensors were found to be 270Ω, 316Ω, 13.7kΩ, and 16.5kΩ.

2.2.3 Flow Sensor Characterization

The flow sensing capability of the four sensors was measured in salt water using a voltage-controlled impeller pump to provide a variable, continuous fluid flow through the flow chamber. Figure 2.6 shows the measured voltage versus time for the SWCNT/PDMS sensor with lowest electrical resistance (270Ω). This measurement shows that the average voltage measured between the two electrodes on the SWCNT/PDMS film surface is on the order of 1mV and the magnitude changes as the flow rate is changed by controlling the pump voltage. The data in Figure 2.6a shows that as the pump voltage is incrementally increased, the voltage difference between the two electrodes also grows. The changes in potential are on the order of 10-20μV per 2V increase in the applied pump voltage (see Table 2.1 for corresponding flow velocities). At the minimum flow setting (6V), the sensor output is approximately 470μV, while for a pump voltage of 12V, the sensor output is 570μV. As the flow rate is then decreased in the latter half of this measurement, the voltage difference also decreases. In addition to the changes in potential upon changing the flow speed, the voltage value also drifted. This effect is attributed to the equilibration of the sample in the electrolyte fluid.

(a)

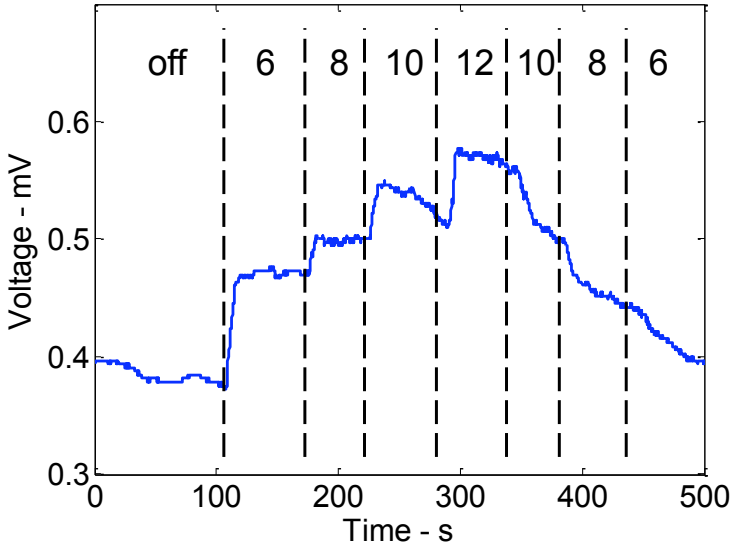

(b)

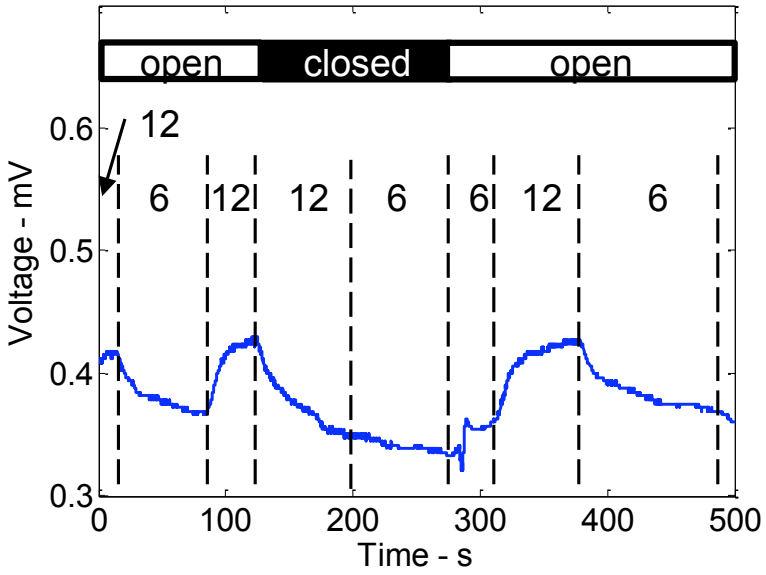

Figure 2.6. (a) Measured sensor voltage versus time for varying flow rates controlled by the pump voltage (values listed are in Volts). (b) A second measurement with the same sensor was used to correlate voltage to both the flow velocity (open valve) and the pump motor speed with no flow (closed valve).

While the measurements in Figure 2.6 show a relatively slow speed of response, especially when comparing to previous works, the time to reach a new steady flow rate is on the order of tens of seconds. This same delay was also seen in the flow velocity (dynamic pressure) measurements and might be attributed to the large total volume (1L)

of water circulating in the flow chamber. Although this needs further investigation, a smaller flow volume might reduce the time lag associated with changing the flow speed and might provide a more suitable method for characterizing the speed of response of the sensor.

The first measurement showed some indication that the sensor can produce a voltage in response to varying flow speeds (and pump motor speeds) controlled by the pump voltage. In order to confirm that these changes are in fact due to the change in flow rate and are not artifacts of the pump motor operating at a higher motor speed, we performed a second measurement of sensor voltage in which the valve in the flow circuit was open and closed separately from prescribing the pump voltage. With the valve open, the voltage developed across the sensor increased with increasing flow rate and decreased as the flow was slowed. However, when the valve was closed, the sensor voltage did not change with changes to the pump voltage. This result demonstrates that the motor speed of the impeller pump is not the source of the measured signal. Instead, the result indicates that variations in the flow velocity account for changes to the signal. The data in Figure 2.6b, however, also show that the total variation in the magnitude of the sensor signal (~60μV) has decreased from the values shown in Figure 2.6a. We later observed that one electrode of this specific sensor began to delaminate from the SWCNT/PDMS surface and we believe that the reduced contact may have altered the measured output.

Figure 2.7 shows the average change in voltage relative to a zero flow condition for the four different fluid velocities (pump voltage settings). At the lowest flow velocity of 96.1 mm/s, a flow-induced voltage change of 100 μV was observed. As the flow speed in the chamber was increased, higher changes in voltage were measured. For 131 mm/s, 143 mm/s, and 191 mm/s, voltage changes of 125 μV, 175 μV, and 195 μV were seen respectively. The solid red line in Figure 2.7 shows that the measured changes in voltage versus flow rate obey a linear relationship. In order to determine how well this linear trend line approximates the performance of our sensor, the coefficient of

determination (R^2) is computed and found to be ~ 0.97. Since this R^2 value is close to 1, it can be said that the measured output of the flow sensor is modeled well in the trend line. Therefore, the slope of this trend line can represent the sensitivity of the sensor. Using this linear relationship, the sensor's sensitivity is evaluated and found to be 1.06 $\frac{\mu V}{mm/s}$.

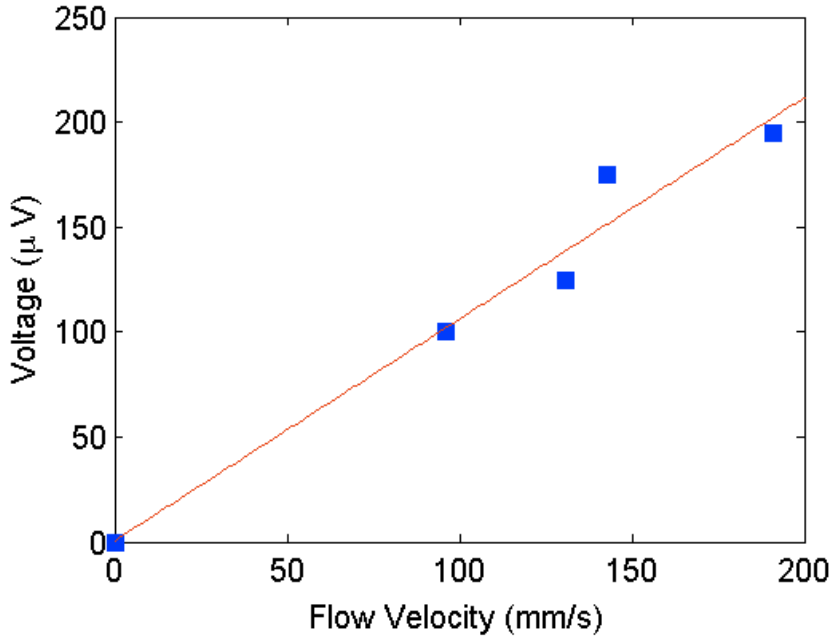

Figure 2.7. Average change in voltage (μV) as a function of the fluid velocity (mm/s)

In addition to voltage, the sensor current was measured under varying flow conditions. However, unlike voltage, the average current did not vary when the flow velocity was changed. Instead, only the amplitude of the noise level grew as a function of the pump speed. This result can be explained by the fact that the impedance of the sensor in salt water includes both the resistance of the sensor surface as well as the electrical resistance through the electrolyte between the electrodes. Since the EIS measurement (Figure 2.5) of the sensor in salt water demonstrated that this pathway is in fact more conductive than the sensor surface itself, the current measured through the sensor will

be less than that generated through the water. Therefore, measurements of current did correlate to the flow conditions imposed in the chamber.

Separately, voltage measurements of the three other sensors were performed under the same flow conditions. However, the response of these sensors as well as the uncharacterized SWCNH/PDMS sensors did not match what was seen with the least resistive sensor. For each of these trials, a small voltage (a few mV) was measured between the electrodes. This voltage did exhibit considerable drift during the measurement, though no distinct changes in potential were observed as a result of changing the prescribed water flow. This lack of electrical response in the SWCNT/PDMS sensor due to changes in flow is attributed to the insufficient exposure of carbon nanotubes on the surface of our PDMS substrate, a consequence of the fabrication method. On the other hand, the single walled carbon nanohorns (SWCNH) sensors contain a larger amount of PDMS on the surface due to the fabrication method but also because of the inherent property of SWCNH to accumulate and form clumps. This agglomeration of SWCNH makes it difficult for the carbon material to pass through the filter during the fabrication process and as a result is largely surrounded by the PDMS [59, 60]. Therefore, our next goal was to focus on increasing the interaction between the carbon nanomaterial/PDMS film and the fluid.

2.2.4 Oxygen Plasma Treatment

Studies have shown that a hydrophobic polydimethylsiloxane (PDMS) surface can be made hydrophilic through oxygen plasma exposure and be used to perform tasks such as forming permanent bonds with itself or other surfaces such as glass and facilitating micro-channel filling with aqueous solutions. In addition, masking with a stencil can also selectively activate PDMS surfaces in order to create a pattern of hydrophilic and hydrophobic sections on a surface [61-63]. As mentioned earlier, the sensors fabricated by our team are composite carbon nanomaterial/PDMS films. The effect of oxygen plasma on a hydrophobic surface such as PDMS is of importance in our work, because

the sensors fabricated by our team use a PDMS substrate as the base surface. Creating a hydrophilic surface would attract greater amounts of water toward the embedded carbon material and as a result would improve the response of the flow sensors. Therefore, in order to open the possibility of increasing the interaction between the protruding carbon nanomaterial and the water phase, the sensor's PDMS surface was oxygen plasma-treated.

Plasma treatment of the composite carbon nanomaterial/PDMS films was carried out using a tabletop plasma cleaner (PDC-001, Harrick Plasma). Specifically, a SWCNH/PDMS sensor and a SWCNT/PDMS sensor were plasma cleaned. In order to study the effect of surface wettability of our films, the surface was exposed to oxygen plasma on the highest setting at 29.6 W for a duration of 60 minutes and then tested in different flow velocities. The flow-induced velocity of the plasma-treated sensor was then compared to the sensing response of the same untreated sensor.

The flow sensing capability of the plasma treated sensor was measured in salt water using the same experimental setup in our initial tests. As shown in Table 2.1, four flow velocities were delivered using an impeller pump. Figure 2.8 compares the measured voltage versus time for an untreated SWNCH/PDMS sensor and an hour-long plasma-treated SWCNH/PDMS sensor. The measurement displayed on this plot shows that the average voltage measured between the two electrodes on the treated sensor's surface showed a much improved (higher and more distinct) voltage response (blue trace) when compared to its changes in potential before plasma treatment (red trace). As in our initial tests, the voltage response of the plasma-cleaned sensor shows that as the pump voltage is incrementally increased, the voltage difference between the two electrodes also grows. The changes in potential are on the order of 250 μV per 2V increase in the applied pump voltage (see Table 2.1 for corresponding flow velocities). At the minimum flow setting (6V), the sensor output is approximately 1.5 mV, while for a pump voltage of 12V, the sensor output is 2.25 mV. As the flow is turned off in between each interval, the measured voltage also drops down toward its initial baseline voltage.

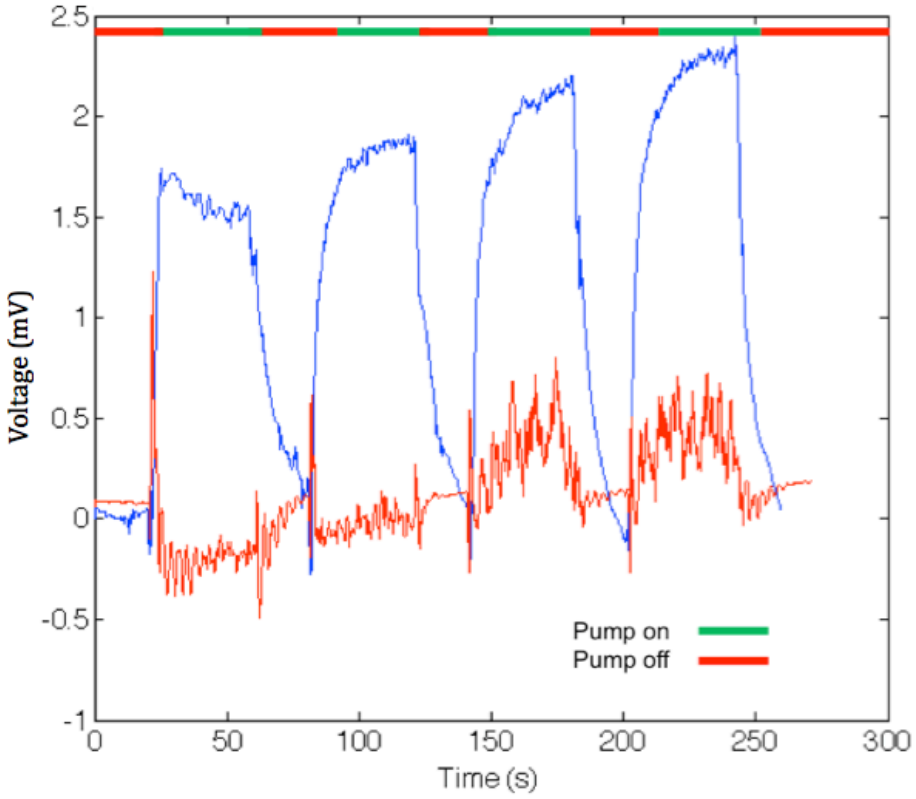

Figure 2.8. Measured sensor voltage versus time for varying flow rates controlled by the pump. Untreated SWCNH/PDMS sensor (red trace) shows no distinct changes in potential as a function of varying flow velocities. Plasma-treated SWCNH/PDMS sensor shows improved and distinct changes in potential as the flow velocity changes.

Figure 2.9 compares the measured voltage versus time for an untreated SWNCT/PDMS sensor and an hour-long plasma-treated SWCNT/PDMS sensor. The measurement displayed on this plot shows that the average voltage measured between the two electrodes on the treated sensor's surface showed a higher voltage response (blue trace) when compared to its changes in potential before plasma treatment (red trace). The voltage response of the plasma-cleaned sensor shows that as the pump voltage is incrementally increased, the voltage difference between the two electrodes also grows, but unlike our initial tests, the last three voltage outputs are all approximately 25 mV. This increase in flow-induced voltage and saturation at higher velocities was a phenomenon seen in previous work by Cao, *et al*. [56].

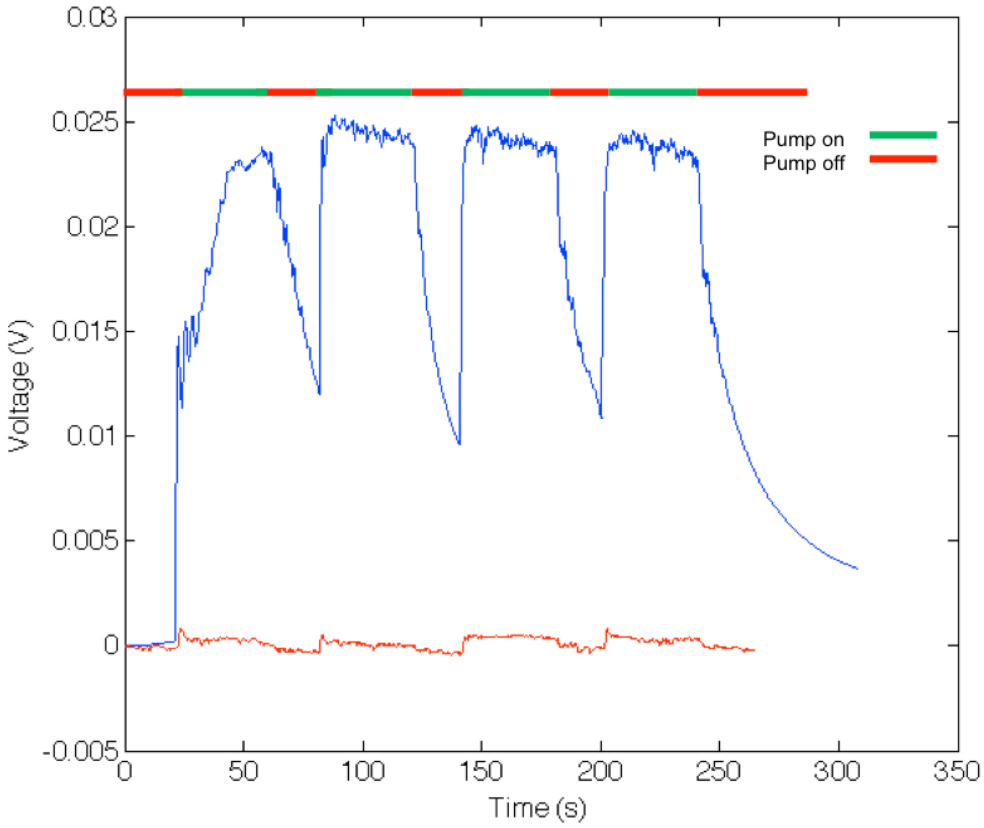

Figure 2.9. Measured sensor voltage versus time for varying flow rates controlled by the pump. Untreated SWCNT/PDMS sensor (red trace) shows small changes in potential as a function of varying flow velocities. Plasma-treated SWCNT/PDMS sensor shows improved changes in potential as the flow velocity changes.

Rendering the surfaces of the SWCNT/PDMS and SWCNH/PDMS sensors hydrophilic through plasma cleaning shows to improve the voltage response of both sensors. Prior to plasma cleaning, the SWCNT sensor generated voltages of 2.5-5 mV per flow velocity increment. Oxygen plasma cleaning of the sensor increased the sensor's sensitivity by producing changes in voltage of 22.5 -25 mV. Conversely, the SWCNH sensor showed no distinct changes prior to plasma treatment (due to the lack of protruding carbon nanohorns on the PDMS surface), but post plasma-treatment showed a potential change of 1.5 mV at the lowest flow velocity and 2.25 mV at the highest flow velocity. The larger amount of carbon material protruding above the PDMS surface of

the SWCNT/PDMS film in comparison to the SWCNH/PDMS film supports this greater increase in sensitivity of the SWCNT sensor. These tests help demonstrate that in addition to the flow-induced voltage being a function of the flow rate, the ionic conductivity of the liquid, and the amount of SWCNT/SWCNH surface coverage, the hydrophilicity of the carbon nanomaterial/PDMS film surface also plays a significant role in improving the sensitivity of the sensors.

2.3 Summary and Conclusions

In this study, two sets of composite carbon nanomaterial/PDMS films (both SWCNT/PDMS and SWCNH/PDMS) were prepared based on techniques developed in previous studies. These techniques produced samples with considerable levels of surface coverage. Both microscopy and electrical resistance measurements of the finished samples showed that the surface film is not purely CNT or CNH but is also comprised of the insulating PDMS layer. Initially, in order to characterize the carbon nanomaterial/PDMS films, sensors were developed from only the SWCNT/PDMS samples because of their higher exposure of carbon nanomaterial on the surface. EIS measurements of the electroded sensors showed that in water, conduction between the electrodes occurs both across the resistive composite carbon film and through the conductive electrolyte. Since previous studies demonstrated that sensor voltage is dependent on the salt concentration (polarity) of the flowing water, understanding the electrical impedance of the sensor in water is important. Voltage measurements across the two electrodes of the initial SWCNT/PDMS sensors showed varying responses when tested in flowing water. While one sample showed small, but measurable, changes in voltage (~10-100μV), the other three demonstrated no correlated changes in voltage to varying flow conditions. This inconsistency is attributed to the fabrication method, which can result in insufficient exposure of carbon material on the surface of our PDMS substrate. For the working SWCNT/PDMS sensor though, these flow-

induced measurements compare well to the changes in potential initially measured by Gosh.

Our next set of experiments focused on improving the sensing capability of the sensors by increasing the interaction between the carbon nanomaterial/PDMS film and the electrolyte fluid through oxygen plasma treatment. Plasma treatment of a SWCNT/PDMS sensor and a SWCNH/PDMS sensor were conducted in order to render the PDMS on the surface hydrophilic and in turn pull more fluid towards the carbon material. Measurements across the two electrodes of SWCNT and SWCNH sensors showed an improvement in the flow-induced voltage. The SWCNT/PDMS films showed an average increase in voltage of approximately 20 mV but saturation at the higher flow velocities. Overall, the plasma treatment seemed to improve the sensitivity of the SWCNT/PDMS sensor from $\sim 27.2 \frac{\mu V}{mm/s}$ to $\sim 139.8 \frac{\mu V}{mm/s}$. The SWCNH/PDMS films, which likely have an insufficient amount of exposed carbon nanohorns, showed distinct increases (compared to pre-plasma treatment) in the measured voltage and generated flow-induced voltages of 1.5-2.25 mV. As in the SWCNT/PDMS films case, plasma treatment of the SWCNH/PDMS films resulted in an improved sensitivity but with a far smaller increase from $\sim 2.7 \frac{\mu V}{mm/s}$ to $\sim 12.2 \frac{\mu V}{mm/s}$.

Our future efforts in this work are to develop a better understanding of how surface structuring of the carbon nanomaterial affects both the electrical impedance of the material and the sensor response. Through SEM, XPS, and AFM measurements of the composite film, we aim to refine our fabrication methods for producing more conductive and hydrophilic films that increase the interaction between the carbon nanomaterial and the water phase. Moreover, the effect of a range of flow velocities and flow types will need to be examined in order to gain a better understanding of the flow sensing capability of these carbon nanomaterial sensors. In this fashion, the transduction mechanism of CNTs and CNHs can then be compared to other carbon materials such as carbon peapods or even graphene.

Chapter 3

Aquatic Flow Sensor using an Artificial Cell Membrane

In our group's previous work, hair cell inspired gel-supported, artificial lipid bilayers were encased in flexible substrates and used as airflow sensors. In response to an applied airflow, the artificial hair cell vibrated and caused a picoamp-level electrical current across the lipid bilayer. Specifically, the measured picoamp-level current was shown to increase in amplitude during airflow over the artificial hair. As in our previous study, the sensor presented in this work uses an artificial cell membrane as a mechanoelectric transduction element, but unlike the air flow sensor, it is developed to endure and sense in an aquatic environment. This study presents the design, fabrication, and characterization of a flow sensor that will help close the loop between the sensing mechanisms and control strategies that various animals use to sense stimuli in aquatic environments, ranging from the fluid-filled structure of the human inner ear to our planet's vast bodies of water. The flow sensing system is fabricated with a durable, artificial bilayer that forms at the interface between lipid-encased aqueous volumes contained in a flexible encapsulated polyurethane substrate. In order to understand the response of our bio-inspired sensor, flow experiments and studies are conducted by submerging the sensor in a flow chamber and subjecting it to both fluid and mechanical excitation.

3.1 Materials and Methods

3.1.1 Sensor Description and Substrate Fabrication

The bio-inspired hair cell aquatic flow sensor presented in this work uses the transduction property of artificial lipid bilayers that are encased in flexible substrates. As shown in Figure 3.1, two lipid-encased aqueous droplet volumes, consisting of phospholipid vesicle solution are connected at the interface between the two compartments. In order to help create the self-assembly of the phospholipids, both compartments are filled with an immiscible oil, hexadecane (99%, Sigma) before pipetting 400 nL of vesicle solution in each compartment. The vesicle solution is composed of 2 mg/mL solution of diphytanoyl phosphocholine (DPhPC) vesicles (Avanti Polar Lipids, Inc.) in 500 mM KCL (Sigma), 10 mM MOPS (Sigma), and ph 7 buffer solution [54].

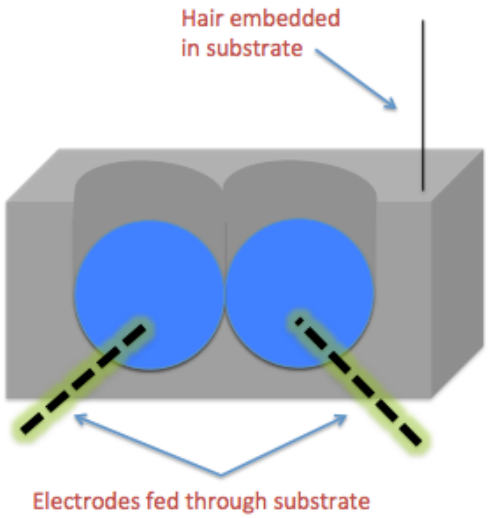

Figure 3.1. A cross-sectional schematic view of the flexible polyurethane substrate used to encase the artificial lipid bilayers. Electrodes that insert through the bottom of the substrate and make contact with each aqueous volume enable electrical measurements. An artificial hair is embedded in the substrate.

The substrate used in this work is inspired by the geometry and design of the substrates used to characterize our artificial, membrane-based hair cell sensors in our previous work [43, 44, 53, 54]. The first step of the fabrication process involves creating a computer-aided design (CAD) model of the desired substrate mold. The next step is to create a numerical control code using the computer-aided manufacturing (CAM) feature of the CAD program in order to upload it onto a computer numerical control (CNC) machine. Using the CNC, a mold for the substrate is machined out of clear acrylic (PMMA). This mold is used to create the polyurethane base substrate. The top surface geometry of this base substrate is shown in the top left of Figure 3.2 and is indented into the top surface using a positive polyurethane mold made from a CNCed acrylic mold. Therefore, the fabrication of the substrate involves a double molding process.

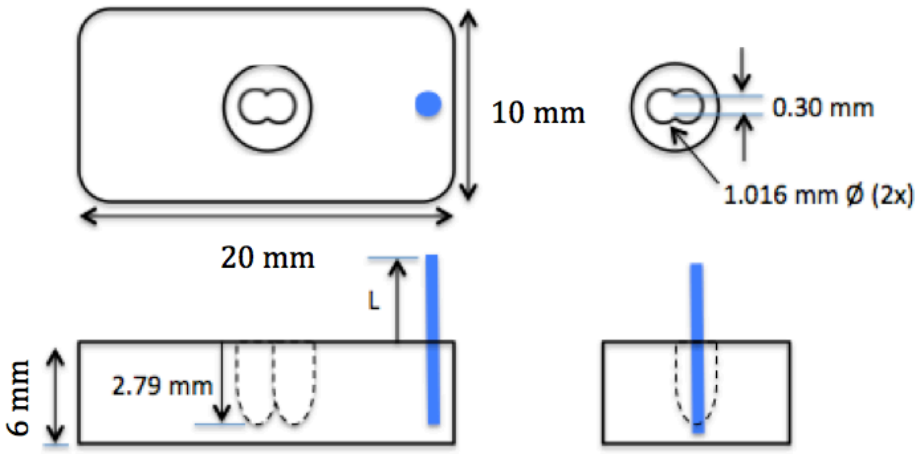

Figure 3.2. A detailed drawing of the polyurethane substrate with an embedded hair: top view, detailed view of housing chambers for oil and aqueous phases, front view, and side view

The final substrate is made from clear and flexible polyurethane (ClearFlex, 50, Smooth-On, Inc.) and as briefly explained above is fabricated using a double molding process. Polyurethane is chosen as the substrate material because it will not absorb the oil or aqueous phase used for bilayer formation. The fabrication process begins by pouring premixed polyurethane in the acrylic negative mold. Prior to pouring, the mold is

sprayed with mold release (Smooth-On, Inc.) in order to allow for easy removal from the mold. In order to degas the polyurethane-filled negative mold, it is placed in a vacuum. After curing the polyurethane-filled mold on a hot place at 80-85 ^{o}C for 35-40 minutes, the positive mold made from polyurethane was released.

Using a CNCed acrylic mold, the substrate base is created by using the same polyurethane molding process used to create the positive mold. As described above, the premixed polyurethane is poured into the mold and degassed. Next, the polyurethane positive created in the first step is sprayed with mold release and placed on top of the uncured polyurethane-filled substrate mold. Placing the positive on top allows for the top surface compartmental geometry of the substrate to form. Once released from the positive and negative mold, the final substrate serves as a housing for the lipid bilayers and also allows for the formation and regulation of the bilayer through an applied mechanical force. Specifically, the regulated attachment method (RAM) is used [43]. This method allows for the flexible substrate to be squeezed in order to separate the droplets. Separating the droplets allows for monolayers to form in each aqueous volume. On the other hand, when the substrate is released, the droplets are brought together and within a few seconds, a bilayer is formed [43]. As shown in Figure 3.1, in order to measure the current across the bilayer during bilayer formation and later during flow tests, silver-silver chloride (Ag/AgCl) electrodes are fed through the substrate into each aqueous droplet. The electrodes are prepared by chloriding 125 $\boldsymbol{\mu m}$ silver wire (Goodfellow) in household bleach until they turn dark gray in color (after ~ 30-60 minutes). Once chlorided, the electrodes are rinsed in water. The electrode ports on the substrate are created using a 300 $\boldsymbol{\mu m}$ diameter drill bit (McMaster-Carr Inc.). The use of silver-silver chloride electrodes results in an efficient ion exchange between the electrodes and prevents the formation of an electrical double layer on the surface of the electrodes. Therefore, the electrode-electrolyte interface in each compartment has negligible resistance and capacitance values. Additionally, the two resistances of the electrolyte solution can be added in series to obtain an equivalent resistance. Figure 3.3 shows this equivalent resistance, R_s as well as the overall simplified circuit model in

which ion flow is only affected by the bilayer interface (resistive and capacitive terms) and electrolyte solution.

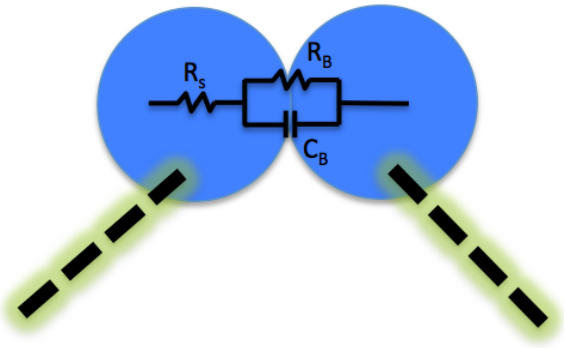

Figure 3.3. A simplified circuit of the conductive pathway between the two electrodes shows the electrical resistance of the electrolyte solution, R_s and the capacitive and resistive nature of the lipid bilayer interface

The artificial hair cell sensor uses a 1080 carbon steel spring-back wire (McMaster-Carr, Inc.) with a 304.8 μm diameter as the artificial hair. As shown in Figure 3.1, the hair is embedded in the polyurethane substrate. This differs from previous work where the hair sat in a volume of polymeric hydrogel. But recently, by mechanically stimulating the hair, it has been demonstrated that the hair does not need to be physically attached to the bilayer to see a response, but instead can be embedded in our substrate [64]. The hair is embedded in the substrate and sealed into position with the use of high-strength glue (Gorrila Glue). Gluing the hair into place creates a fixed boundary condition at the hair's base. This redesigned hair cell sensor has significant implications for future fabrication of hair cell arrays due to the ease of fabrication associated with embedding an array (and varied configurations) of artificial hairs in a substrate as opposed to multiple hydrogel volumes. The hair cell sensors fabricated in this work use hairs of approximately 25.4 mm, 31.75 mm and 50.8 mm in length.

3.1.2 Sensor Encapsulation

In order to test the membrane based hair-cell flow sensor in an aqueous environment, it needed to be encapsulated. The employed encapsulation material needed to be compliant in order to allow for easy squeezing and releasing of the substrate and durable enough to withstand repetitive use. In developing an encapsulation method for the sensor, two primary goals were kept in mind. First, the encapsulation method needed to effectively seal the sensor to prevent oil from leaking out of the substrate or water leaching into the substrate. Secondly, a fluid (prior to curing) material with a lower density than oil needed to be employed. The lower density property of the material will prevent the oil from being pushed out of the compartments, while its fluidity will allow for easy encapsulation of arrays of these artificial hair cells by simply pouring it over the substrate. As show in Figure 3.4, a low density 'skin' was developed using a combination of polyurethane (ClearFlex, 50, Smooth-On, Inc.) and plastic microspheres (Expancel).

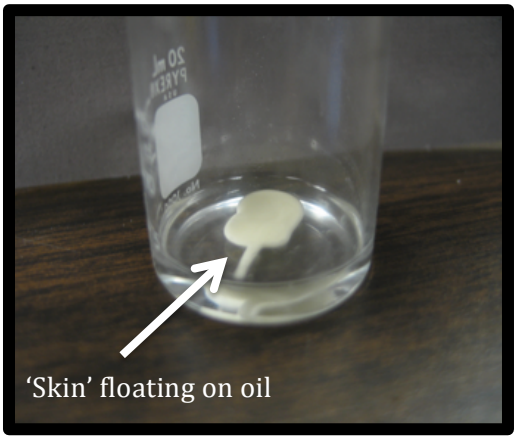

Figure 3.4. A low density 'skin' made from a combination of microspheres and polyurethane sits on a volume of hexadecane oil

Using the density of oil, ρ_{oil}, the density of urethane, $\rho_{urethane}$, and the density of the microspheres, $\rho_{microspheres}$, the relationship shown below was found, where $m_{microspheres}$ and $m_{urethane}$ represent the mass of microspheres and the mass of

urethane respectively. Using this relationship, the minimum amount of microspheres needed to create a 'skin' that floats on top of the oil can be calculated.

$$\frac{m_{microspheres}}{m_{urethane}} > \frac{\frac{\rho_{oil}}{\rho_{urethane}} - 1}{1 - \frac{\rho_{oil}}{\rho_{microspheres}}}$$

Eq 3.1

$$\frac{m_{microspheres}}{m_{urethane}} > 0.014$$

After pouring the 'skin' on top of the sensor substrate in order to encapsulate it, it was found that prior to curing, the 'skin' was partially immiscible with the oil and would therefore absorb the oil present in the substrate compartments. Although the 'skin' was only partially immiscible with the oil and did not prevent curing, it was an issue because the small volume of oil in the compartments resulted in little to no oil left. A larger volume of oil separating the compartments from the 'skin' would solve this absorption issue. By redesigning the substrate to hold a larger volume of oil, the little oil that will be absorbed will not significantly affect bilayer-based sensor. However, since the 'skin' encapsulation method would be of more benefit to sealing artificial hair cell arrays and this work does not include any work with arrays, the substrate presented in this paper is encapsulated by first curing the 'skin' as a cap, placing it on top of the substrate, and sealing the edges with a waterproof urethane-based adhesive. Sealing the substrate in this manner does not require an altered substrate design (in order to hold more oil) and will still result in an effective and compliant 'skin'.

3.1.3 Flow Chamber Description

Tests are performed in a flow chamber with gravity-induced flow. Gravity-induced flow is chosen in order to avoid any electrical interference that may arise with the use of a motor driven pump, such an impeller pump. Reducing the chance of electrical interference in our tests is especially important since the electrical measurements in our study are on the pico-amp level. The flow chamber used is 43.18 cm long and made from rectangular, acrylic tubing (22 mm x 22 mm). The fluid is delivered from an elevated reservoir into the chamber through silicone tubing with an inner diameter of 6.4 mm. In order to keep the gravity-induced flow velocity as consistent as possible, the elevated reservoir was kept at a constant height (initially at ~ 1.5 m and later at ~ 1 m) for each set of experiments and in addition was consistently filled up. A valve is used to control the flow of water and a needle tip is used to direct the flow over the sensor. The sensor is contained in a grounded aluminum block and was placed approximately 14 cm from the entrance of the rectangular tubing. A rectangular window is cut out at the bottom of the chamber at this location in order to insert the aluminum block into the chamber. An image of the flow chamber setup is shown below in Figure 3.5.

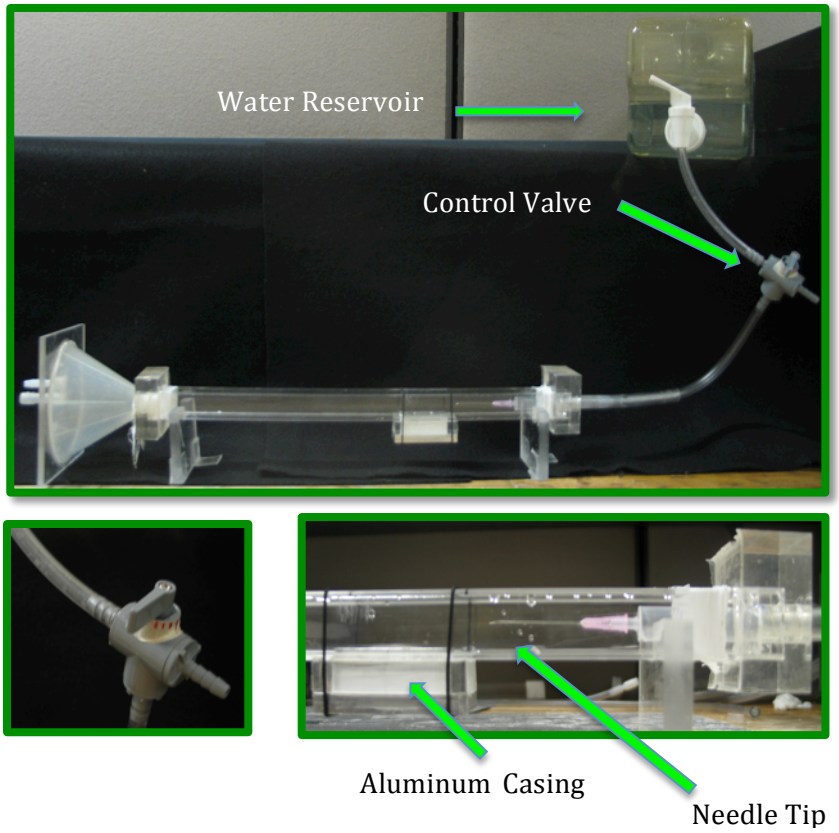

Figure 3.5. Flow chamber setup using a valve-controlled gravity induced flow. A grounded aluminum casing is used to holds the sensor while a needle tip helps focus the flow.

In addition to fluid excitation, the sensing response of the hair-cell sensor while submerged in an aqueous environment is tested through mechanical excitation. Specifically, fluid excitation is carried out through pulse-like flows by quickly opening and closing the valve, while mechanical excitation is conducted by exciting the substrate/test structure with an impulse input.

3.1.4 Experimental Tests for Sensor Measurements

Since previous work in our team did not involve a 'skin'-encapsulated sensor, preliminary work in this study focused on gaining a better understanding of the properties of the encapsulated artificial cell membrane-based sensor through sensing measurements. Specifically, sensing measurements due to pulse-like flows are performed with and without an embedded artificial hair. The embedded artificial is ~ 1 inch in length and completely submerged in water. The goal in testing two sensor configurations is to differentiate the electrical response due to the 'skin' from the response due to the embedded artificial hair and in doing so to improve our understanding of the encapsulated sensor's response.

In the next set of experiments, the dynamics of the artificial membrane-based hair cell sensor are correlated to its sensing response through synchronized current measurements and motion tracking of the hair with a laser vibrometer. Specifically, the laser is focused on the tip of the artificial hair and the hair velocity is tracked during both fluid and mechanical excitation of the hair cell sensor. As mentioned in the previous section, flow tests are conducted by quickly opening and shutting off a valve to deliver a pulse-like flow over the hair cell sensor surface. On the other hand, mechanical excitation of the substrate/chamber fixture is carried out by delivering an impulse on the flow chamber using an impact hammer.

3.1.5 Electrical and Laser Vibrometer Measurements

The formation of a bilayer in our bio-inspired sensor was verified through the measured current induced (across the bilayer interface) by a triangular waveform voltage (10 mV, 20 Hz) outputted by a Hewlett Packard 3314A function generator. This external voltage was only applied to measure the capacitance (size) of the bilayer. The external triangular waveform is then turned off in order to allow for sensing measurements. In

doing so, a steady-state, baseline current at 0 pA (with respect to time) is achieved. Using an AxoPatch 200B patch clamp amplifier (Molecular Devices), a DC potential is applied across the membrane during flow tests and changes in flow-induced current due to flow over the sensor are measured. The device is controlled with AxoScope 10 software (Molecular Devices) and is specifically intended for low-level current measurements at high sampling frequencies. It uses a headstage unit with built-in cooling to provide measurements with low noise levels. In order to further enhance the current measurements by reducing the noise level in the measurements, the headstage is encased in a grounded aluminum shell and placed away from the flow test setup. Measured currents are sampled at 50 kHz and are converted to a digital signal using a DigiData 1400A (Molecular Devices) data acquisition software and then recorded in the Axoscope software. Laser vibrometer tests are conducted by focusing the laser on the tip of the hair and tracking the hair velocity using a PSV-400 (Polytec) laser vibrometer. A frequency range of 50 Hz – 4 KHz and a sample frequency of 6 KHz were used for all measurements. The device is controlled and the recorded data is processed with PSV software.

3.2 Results and Discussion

3.2.1 'Skin' Encapsulated Substrate

Prior to being placed in the flow chamber, bilayer formation is carried out in the 'skin'-encapsulated substrate. This is done in order to verify that a bilayer can be formed in air. Using a micromanipulator as shown in Figure 3.6, the substrate is squeezed in order to separate and electrically isolate the lipid-encased droplets from each other. This is verified from having a small (negligible) current measurement across the electrodes. However, when the substrate is slowly released, the two droplets come into contact and begin forming a lipid bilayer at the interface of the two compartments. Specifically, by gradually releasing the substrate, the two monolayers form a thinned, two-molecule thick bilayer structure [43, 54, 65]. This increase in the bilayer size is

directly related to an increase in the measured square-wave capacitance across the bilayer [44]. The capacitance of an artificial cell membrane can be estimated in real-time from real-time current measurements. The capacitance can be estimated by using the current-voltage relationship for a capacitor. This relationship is displayed below and helps to show that the application of a constantly changing voltage (decreasing or increasing) across a capacitor will result in a steady-state current, I, that is proportional to the capacitance, C, and the rate of voltage change, dV/dt.

$$I = C\frac{dV}{dt} \qquad \text{Eq 3.2}$$

Therefore, in our case, when a symmetric triangle waveform voltage is applied across the electrodes, a square wave current through the bilayer interface (capacitor) is measured. Figure 3.8 shows that as this measured square wave current grows it can be used to verify the increase in capacitance due to the bilayer formation. The two capacitance values of ~ 500 pF and ~ 750 pF shown on the plot are calculated using the relationship shown above and correspond to the two distinct releases of the micromanipulator force against the substrate. The equivalent bilayer area of these two capacitance values can be calculated by using the relationship shown below. The area of the bilayer is computed by using the measured bilayer capacitance and the normalized capacitance, C_{lipids}, of the DPhPC phospholipids (0.6 μF/cm^2) [44, 66, 67]. Therefore, the bilayer areas that correspond to ~ 500 pF and ~ 750 pF are $\sim 8.33 \times 10^{-4} cm^2$ and $\sim 1.25 \times 10^{-3} cm^2$ respectively.

$$A_{bilayer} = \frac{C}{C_{lipids}} \qquad \text{Eq 2.3}$$

In addition to measuring the capacitance, bilayer formation is visually confirmed by using an inverted light microscope. Figure 3.7 shows an image of this visual

confirmation when two droplets come into contact with each other and begin forming a lipid bilayer at the interface.

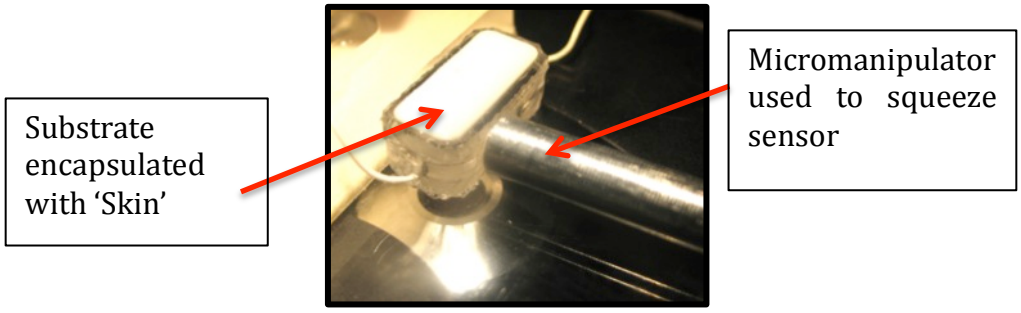

Figure 3.6. Micromanipulator used to apply an external force on the 'skin'-encapsulated membrane-based sensor

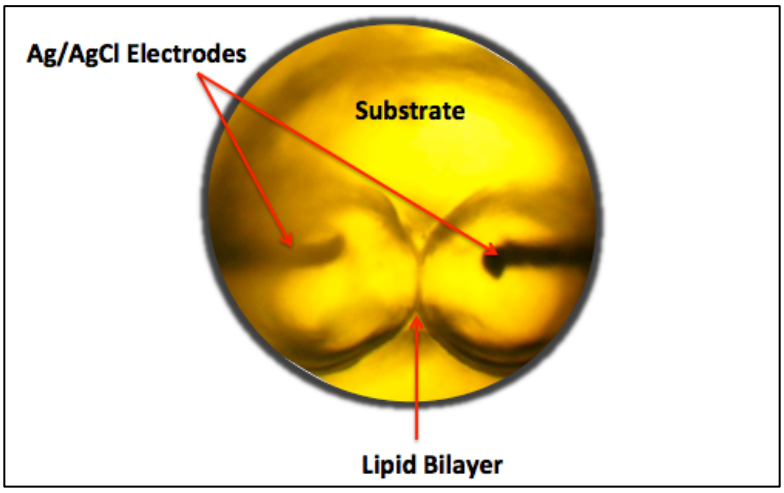

Figure 3.7. Image of bilayer interface formed in a 'skin'-encapsulated sensor

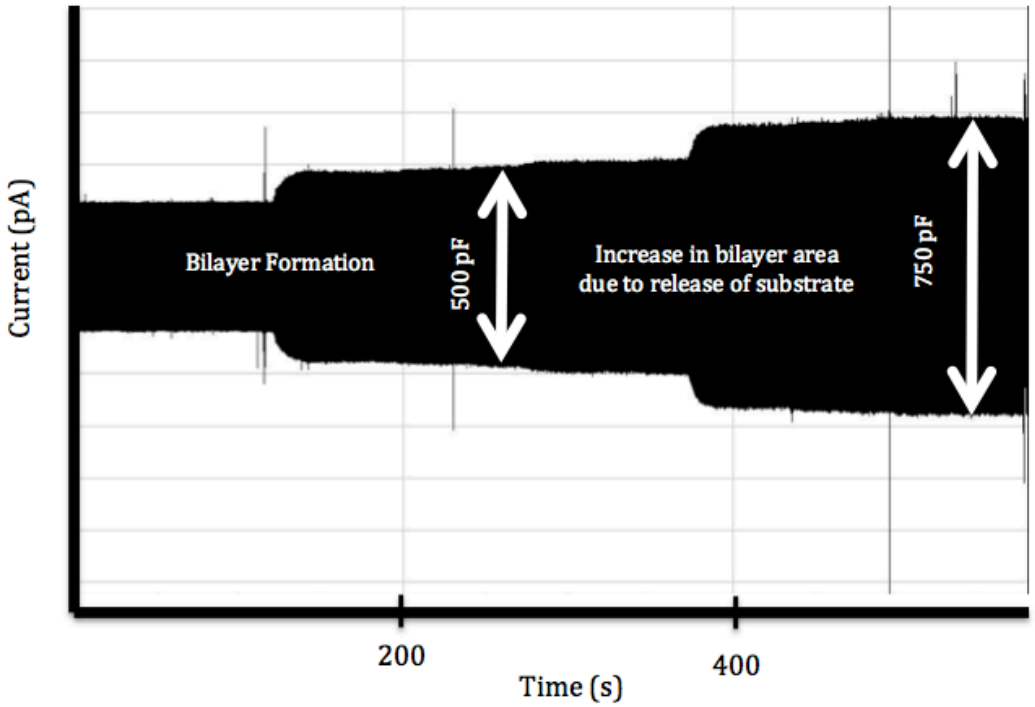

Figure 3.8. The two distinct size increases in current values are directly related to an increase in the measured square-wave capacitance across the bilayer due to the release of the micromanipulator. Releasing the applied force on the substrate results in an increase in the bilayer size.

Once a 'skin'-encapsulated bilayer is formed, the sensor is housed in a grounded aluminum block and placed in the flow chamber for testing. The aluminum block consists of two screws on both its sides in order to allow for the RAM technique to be carried out once the sensor is in the flow chamber. It was shown that the submerged sensor is able to withstand multiple substrate compressions in order to separate and reattach the aqueous volumes for bilayer formation. This confirms the ability to effectively form and hold a stable bilayer while the encapsulated sensor is in an aquatic environment.

3.2.2 Flow Sensor Response as Function of Surface Morphology

The flow sensing capability of the sensor was measured in water using a valve-controlled gravity-induced flow to provide a pulse-like flow through the flow chamber. Figure 3.9 shows a temporal response for the measured current of the 'skin'-encapsulated bilayer without an embedded artificial hair as a pulse-like flow traveled over its surface. As shown on the plot, the background current across bilayer membrane is around 20 pA. However, when a pulse of water travels over the 'skin' ($t \approx 0.09\ s$), it perturbs the surface and we see an increase in the amplitude of the measured current (maximum increase of ~ 80 pA) with no average change. This increase in amplitude is likely due to the transmission of vibrations from the 'skin' to the oil and lipid-encased droplet volumes. Specifically, as shown in our previous work [54], the oscillations in the capacitance (and current) of the bilayer when water perturbs the surface of the sensor, are likely due to the bending of the lipid bilayer. As shown in the plot, the oscillatory current measurements are at a higher frequency when compared to the background current frequency. At approximate $t = 0.12\ s$, when there is no flow over the sensor, the measured current returns to its initial value of approximately 20 pA.

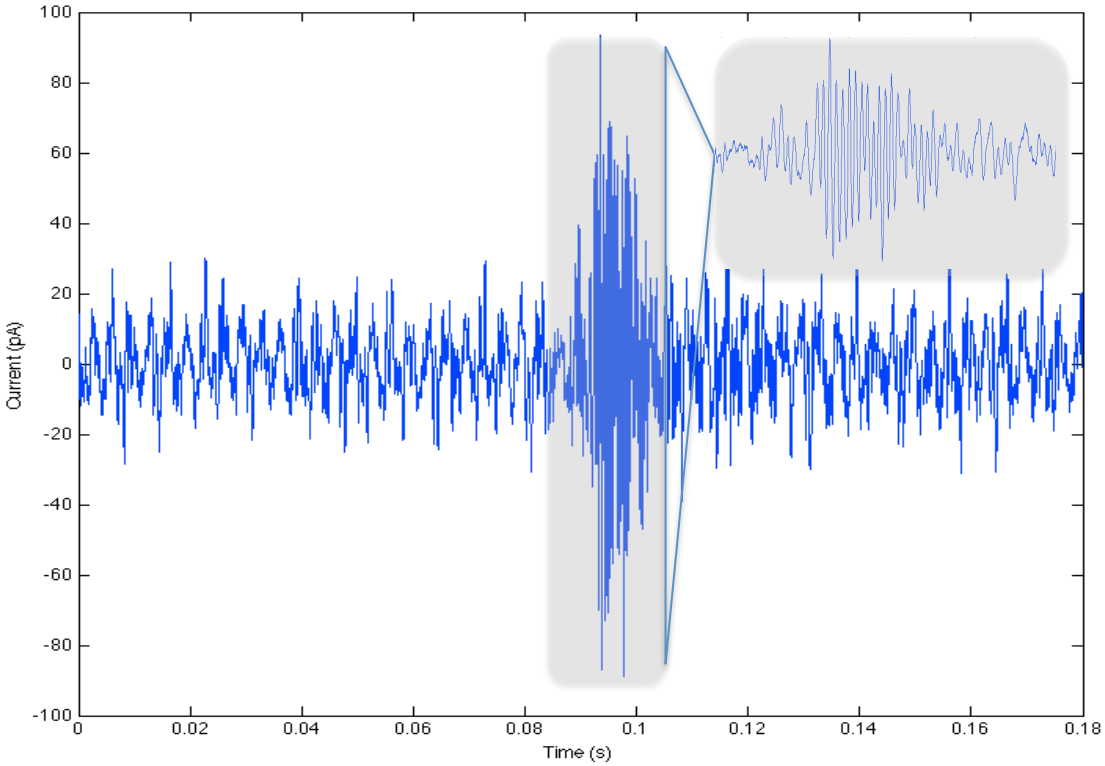

Figure 3.9. The plot shows the measured flow-induced current response of the 'skin'-encapsulated sensor without an embedded hair as a pulse-like flow is delivered over its surface ($t \approx 0.09\ s$)

In comparison, Figure 3.10 shows a response for the measured current of the 'skin'-encapsulated artificial hair cell sensor as a pulse of water travels across the surface. As displayed on the plot, the background current is about 20 pA, but in the presence of a pulse-like flow across the artificial hair cell ($t \approx 0.5\ s$), there is an increase in the amplitude of the current (maximum increase of ~ 80 pA) with no average change in the value. Unlike the sensor with no hair, the oscillations in the measured current are at a lower frequency and take a longer time period to dissipate. At $t \approx 1.3\ s$, when there is no flow over the sensor, the measured current returns to its initial value of approximately 20 pA.

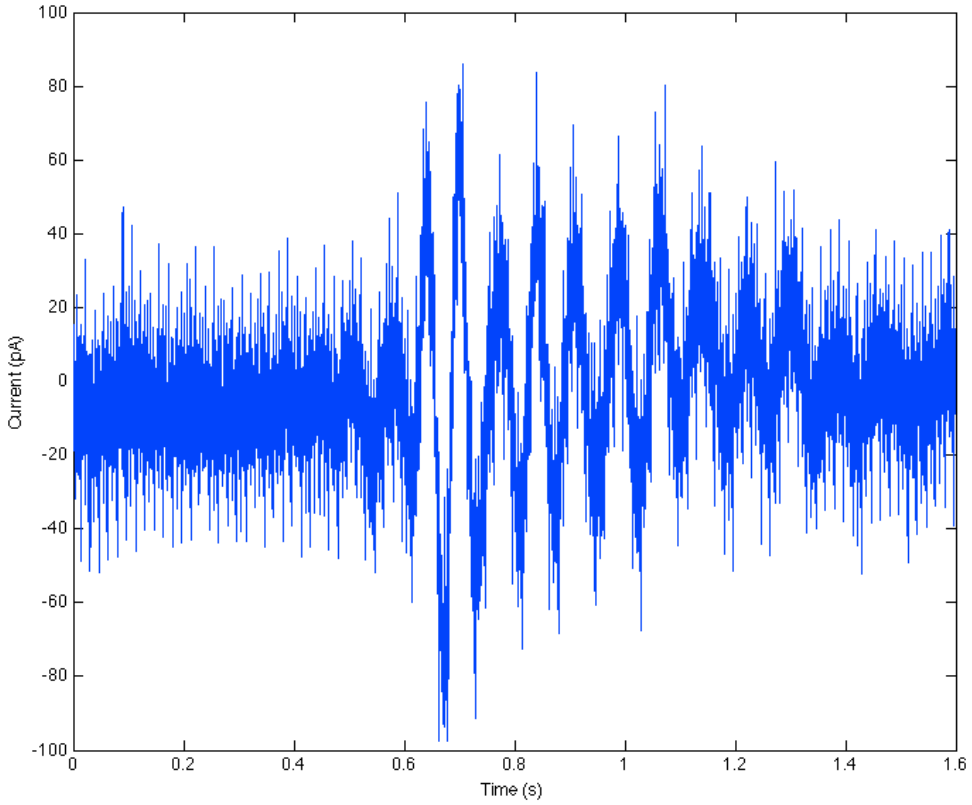

Figure 3.10. The plot shows the measured flow-induced current response of the 'skin'-encapsulated sensor with an embedded hair

Therefore, as an impulse of water hits the embedded artificial hair in our bio-inspired aquatic flow sensor, the lower frequency of oscillation in the current response is most likely correlated to the vibrations of the hair in the flow. Furthermore, the response of the sensor with no embedded hair died out in ≈ 0.03 s, which is significantly shorter in comparison to the hair cell's timeframe of ≈ 0.8 s. This longer dissipation time is likely due to the reduced damping in the hair. The surface of the 'skin' on the other hand is a more damped system and as a result would transmit flow-induced vibrations from skin to the bilayer for a shorter period of time.

Figure 3.11 shows the power spectral densities (PSD) of the sensor's temporal responses in three different scenarios. Specifically, the plot shows the PSD of the 'skin'-encapsulated bilayer without an embedded artificial hair as an impulse of water

travels over it (green trace), the ‘skin’-encapsulated artificial bilayer with no hair and no flow (red trace), and the ‘skin’-encapsulated artificial hair cell under an impulse flow condition (blue trace). The PSD of the current response as a result of flow over the encapsulated bilayer without an artificial hair shows higher amplitudes are present at higher frequencies. This pattern at higher frequencies most likely correlates to the sensor’s high frequency oscillatory current measurements as shown in the temporal response in Figure 3.9. In comparison, the PSD of the measured current response when there is flow over the artificial hair cell sensor, shows a higher amplitude at lower frequencies. As shown in the current response in Figure 3.10, this phenomenon is likely related to the sensor’s low frequency vibrations and current measurements. Comparing these two PSD plots with the PSD of the current response during no flow over the sensor (background current), we are able to confirm that the frequency response of the bio-inspired sensor is a function of its surface morphology.

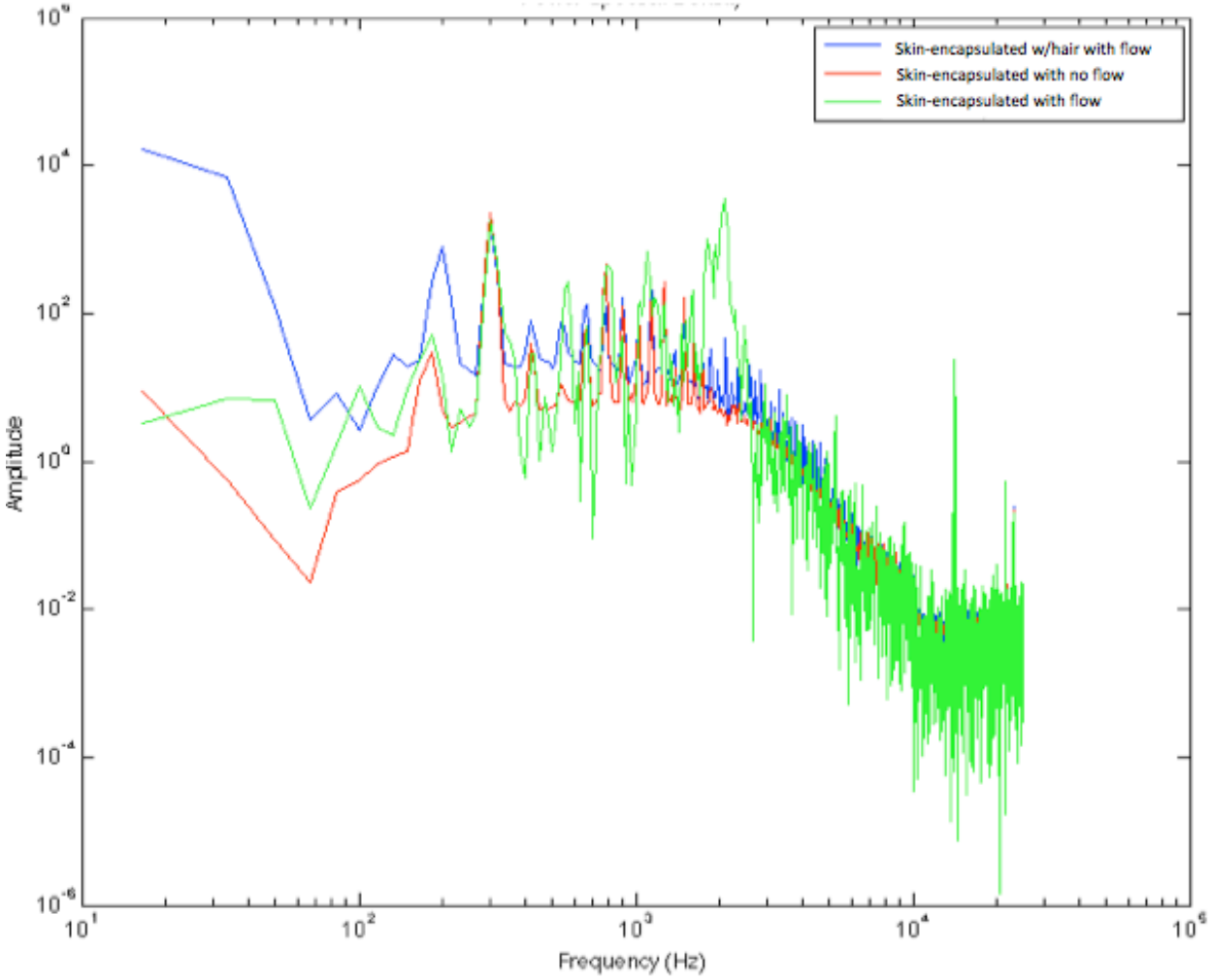

Figure 3.11. The power spectral density of the 'skin'-encapsulated artificial bilayer with no hair and no flow (red trace), of the 'skin'-encapsulated bilayer without an embedded artificial hair as an impulse of water travels over it (green trace), and the 'skin'-encapsulated artificial hair cell under an impulse flow condition (blue trace)

These preliminary tests helped to show that the encapsulated artificial hair cell flow sensor is capable of sensing changes in flow through a mechanoelectrical response and that its sensing capabilities may be altered by varying its morphology and surface topology. Therefore, our next step was to refine our study in order to better understand the sensor's response and dynamics as a function of its surface morphology and structural properties.

3.2.3 Synchronized Current and Laser Vibrometer Measurements

In order to better understand the motion of the hair and the measured current response, synchronized motion tracking of the hair with a laser vibrometer and measurements of current across the bilayer were carried out. In doing so, we hope to better correlate the dynamics of the artificial membrane-based hair cell sensor to its sensing response. The effect of both fluid and mechanical excitation of the hair cell on the sensor's vibration is understood by focusing the laser on the tip of the artificial hair and tracking the hair's velocity. Specifically, in order to avoid any inconsistencies in our measurement due to reflection or refraction off the water, an artificial hair length that allows the tip of the hair to barely protrude from the water surface is chosen, so that the laser can be directly focused on the hair. Therefore, a hair with an approximate length of 31.75 mm is used in our artificial hair cell. Using a model given by Inman [68] for a cantilever beam in bending, the first natural frequency of the artificial hair is found to be ~ 218 Hz. Figure 3.12 below shows a schematic of this test setup and image of the laser focused on the tip of a submerged hair cell sensor.

(a)

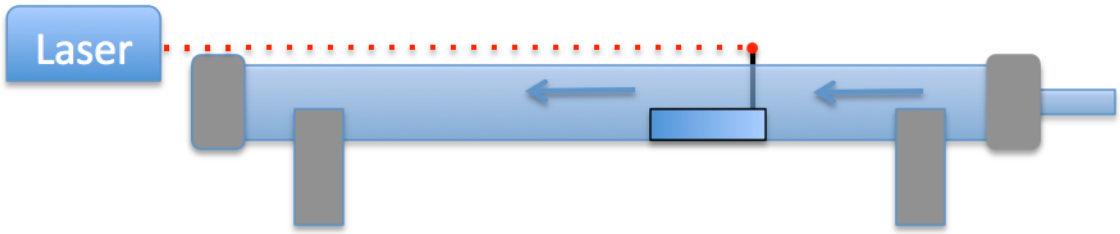

(b)

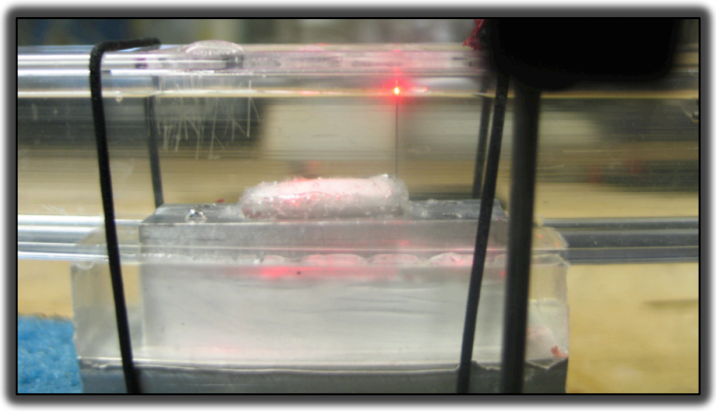

Figure 3.12. (a) Schematic view of the laser focused on the tip of the artificial hair. The 31.7 mm hair barely protrudes the surface of the water as an impulse of flow travels over the surface of the sensor. (b) An image of a submerged artificial hair cell with a laser focused on the tip of the hair

As done in preliminary tests, the flow sensing capability of the hair cell sensor was measured in water through a fluid excitation created by a pulse-like flow (delivered by quickly opening and closing the valve). Figure 3.13 shows two traces: the top plot is the temporal response for the measured velocity of the artificial hair as a pulse-like flow traveled over its surface while the bottom plot is the corresponding temporal response for the measured current across the bilayer. As shown in Figure 3.13 (a), the hair is initially stationary, shown by the small changes in velocity around zero. However, when a pulse of water travels over the hair ($t \approx 0.3\ s$), it vibrates the hair and we see distinct oscillatory changes in the velocity (maximum increase of ~ 2mm/s) of the hair, but with no dc change. These changes in hair velocity are due to the changes in flow over the

artificial hair. At approximate $t = 0.8\ s$, when there is no flow over the sensor, the measured hair velocity returns to its initial value of approximately zero. The corresponding current measurement across the bilayer shown in Figure 3.13 (b), shows the background current is about 25 pA, but in the presence of a pulse-like flow across the artificial hair cell ($t \approx 0.2\ s$), there is an increase in the amplitude of the current (maximum increase of ~ 45 pA) with no average change in the value. At $t \approx 0.4\ s$, when no flow-induced vibrations are transmitted to the bilayer, the measured current returns to its initial value of approximately 25 pA.

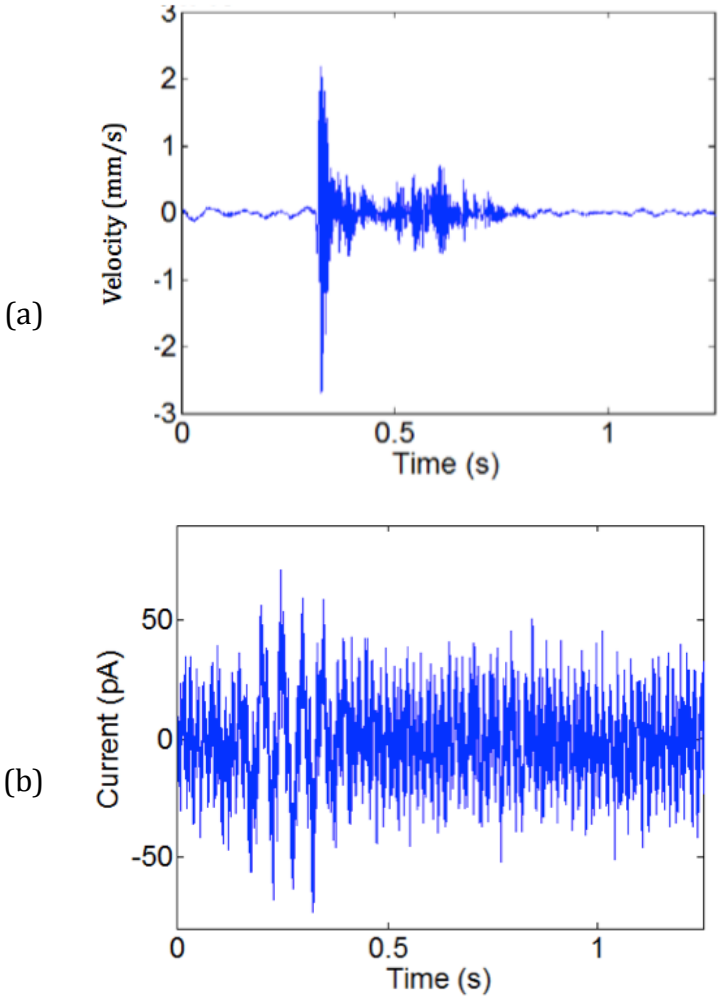

Figure 3.13. (a) The measured hair velocity during flow over the artificial hair cell sensor and (b) the corresponding current response measured across the artificial cell membrane with a 31.75 mm long hair

These change in current occur around the same time period (with a slight mismatch) as the velocity changes in the hair. These simultaneous velocity and current measurements prove that the flow over the sensor affects both the velocity of the hair and the current across the bilayer, however they do not demonstrate whether the changes in current are in fact due to the vibrations of the hair. Therefore, in order to understand the mechanical phenomena for this change in flow-induced current across the bilayer, the next step was to carry out a frequency analysis of these synchronized measurements.

The time domain response of the hair vibration and bilayer current are both converted into the frequency domain using a fast Fourier transform (FFT). Figure 3.14 shows the two FFT traces: the top plot is the FFT for the measured velocity of the artificial hair as a pulse-like flow traveled over the sensor's surface while the bottom plot is the corresponding FFT for the measured current across the artificial cell membrane. The frequency analysis of the hair velocity measurement shows a dominant frequency peak near 216 Hz, which is near the calculated first natural frequency of the cantilever artificial hair. This result shows that the measured oscillations in hair velocity are in fact due to the flow-induced vibration of the artificial hair. On the other hand, the FFT for the measured bilayer current shows four distinct frequency peaks around 94 Hz, 120 Hz, 180 Hz, and 300 Hz. Apart from the 94 Hz peak, the three other frequencies are due to environment's background noise, such as 60 Hz electrical noise. This frequency analysis does not show any distinct frequency peaks near 216 Hz and as a result suggests that the current measured across the bilayer during flow excitation is not correlated to the motion of the hair. This explains the slight mismatch in time periods of the velocity and current changes, because the changes in current are likely due to the vibration of the substrate, which is not picked up by the laser. Therefore, the measured changes in current during the impulse of flow are caused by other excitations in the system, such as the sensor substrate or possibly even the electrodes.

(a)

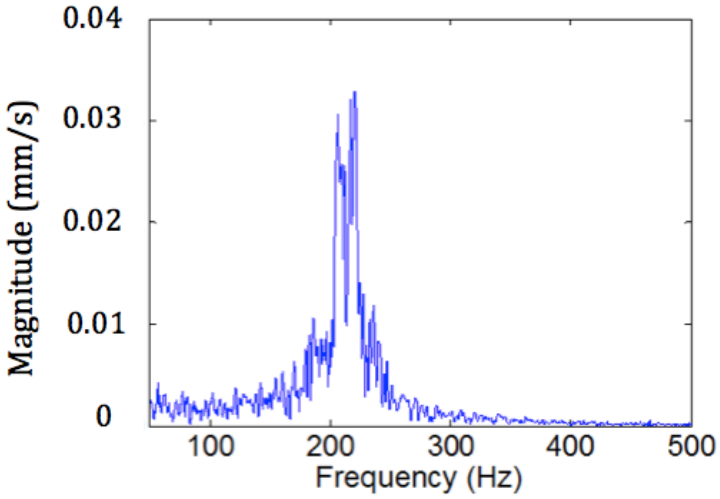

(b)

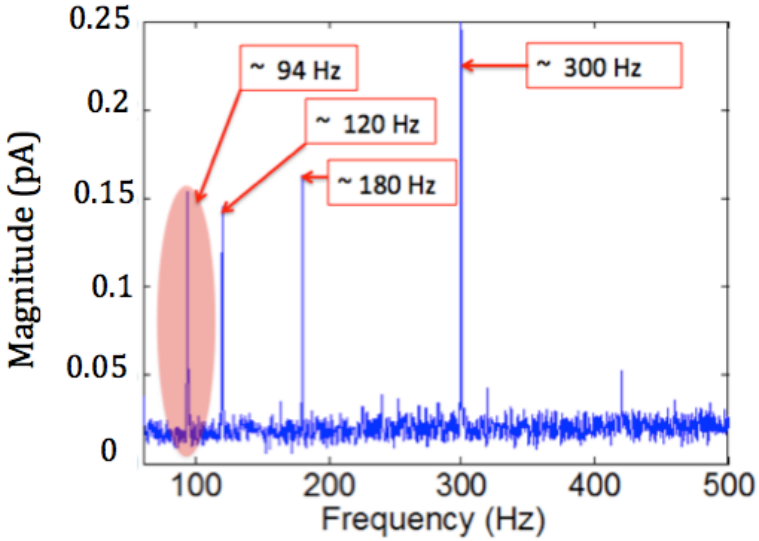

Figure 3.14. The fast Fourier transform (FFT) of (a) the flow-induced hair velocity measurement and (b) the corresponding flow-induced current measurement of the sensor with a 31.75 mm long hair.

The next step in our experimental process was to test the response of our submerged sensor due to a mechanical excitation of the substrate/test structure with an impulse input. In doing so, the goal was to better understand the mechanical coupling between the sensor's substrate and artificial hair. The mechanical impulse excitation was delivered with an impact hammer on the rigid tubing of the flow chamber. A schematic of the setup with the impact location is shown below in Figure 3.15.

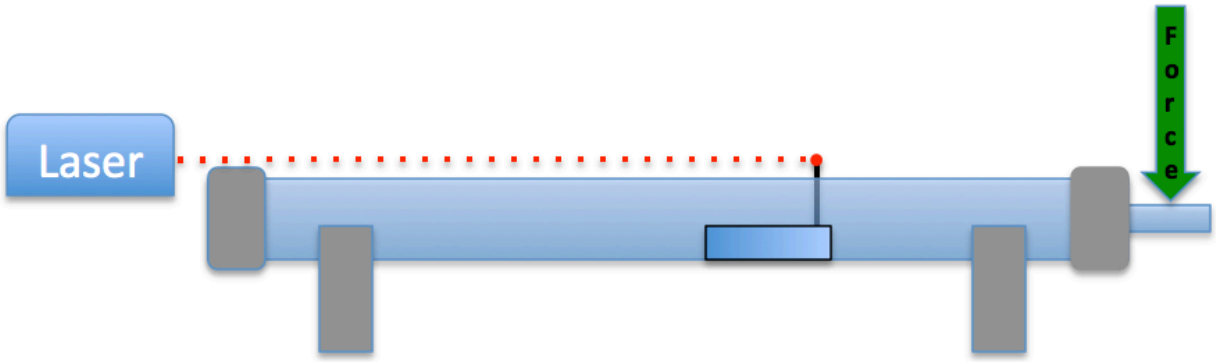

Figure 3.15. Schematic view of the test set up and the location of the mechanical excitation using an impulse hammer.

The two traces shown in Figure 3.16 display the response of the sensor after a single mechanical impulse: the top plot is the temporal response for the measured velocity of the artificial hair as the impulse excitation is transmitted to the base of the sensor while the bottom plot is the corresponding temporal response for the measured current across the bilayer. As shown in Figure 3.16 (a), the hair is initially stationary, shown by a velocity around zero. However, when the mechanical impulse is transmitted from the substrate/chamber fixture to the hair ($t \approx 0.32\ s$), it vibrates the hair and we see distinct oscillatory changes (maximum increase of ~ 2mm/s) in the velocity of the hair, but with no dc change. These changes in hair velocity are due to the vibrations in the submerged sensor substrate. At approximate $t = 0.4\ s$, when the sensor does not experience any vibrations, the measured hair velocity returns to its initial value of approximately zero. The corresponding current measurement across the bilayer shown in Figure 3.16 (b), shows a background current of about 25 pA, but in the presence of a mechanical excitation of the artificial hair cell ($t \approx 0.32\ s$), there is an increase in the amplitude of the current (maximum increase of ~ 25 pA) with no average change in the value. At $t \approx 0.4\ s$, when there is no excitation of the sensor, the measured current returns to its initial value of approximately 25 pA.

(a)

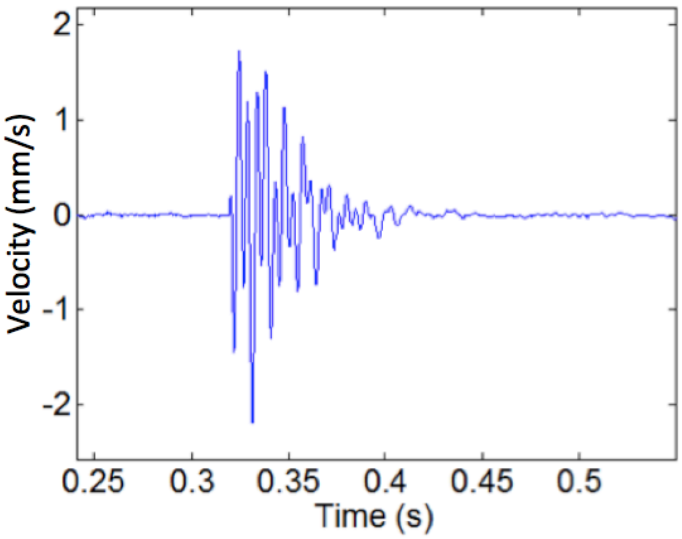

(b)

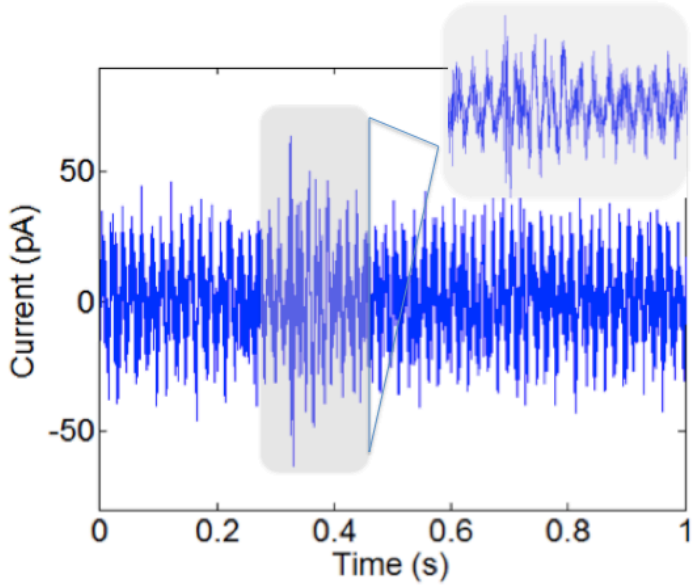

Figure 3.16. (a) The measured hair velocity after a mechanical impulse excitation and (b) the corresponding current response measured across the artificial cell membrane with a 31.75 mm long hair

These changes in current occur in the same time period as the velocity changes in the hair. However, as done in the flow-impulse tests, a frequency analysis of these results is carried out in order to understand if the measured changes in current are correlated to the hair vibrations.

Figure 3.17 shows two FFT traces: the top plot is the FFT for the measured velocity of the artificial hair as the mechanical impulse is transmitted to the base of the sensor while the bottom plot is the corresponding FFT for the measured current across the artificial cell membrane. In addition to the dominant frequency peak around 216 Hz (close to the estimated first natural frequency of the hair), the frequency analysis of the hair velocity measurement also shows a significant frequency at ~ 90 Hz and smaller peak at around 120 Hz. This result shows that the measured oscillations in hair velocity are due to not only the vibration of the artificial hair, but also to the vibration of the substrate/chamber. The FFT for the measured bilayer current does not show any distinct frequency peaks near the first natural frequency of the hair, but similar to flow impulse test, a small but more distinct peak (in comparison to the flow test) around the substrate/chamber frequency at 94 Hz is seen. Therefore, this result suggests that the current measured across the bilayer during a mechanical excitation is not correlated to the motion of the hair, but instead to the vibration of the substrate/chamber. This result also helps to demonstrate that the frequency peak at ~ 94 Hz in the FFT of the flow-induced current response (Figure 3.14 b) confirms that the measured current is in fact due to the vibration of the sensor substrate.

(a)

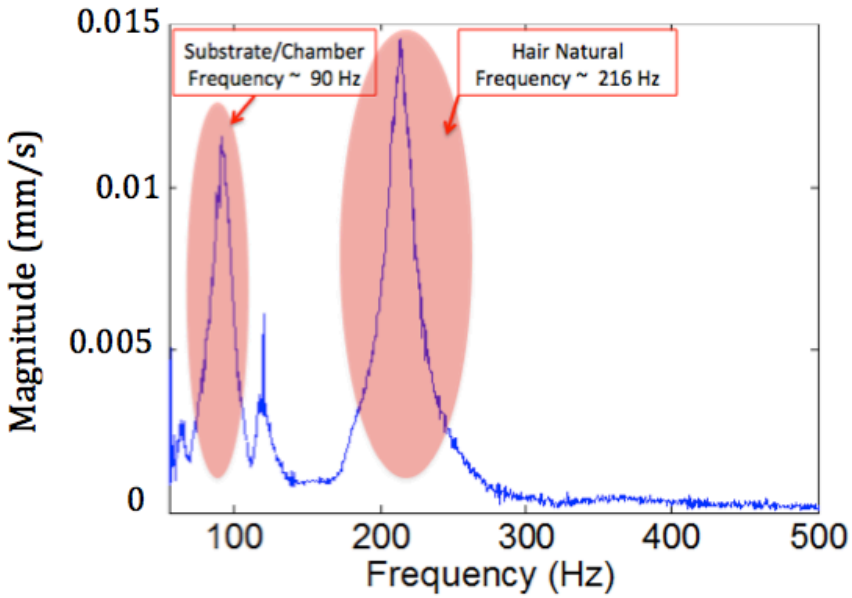

(b)

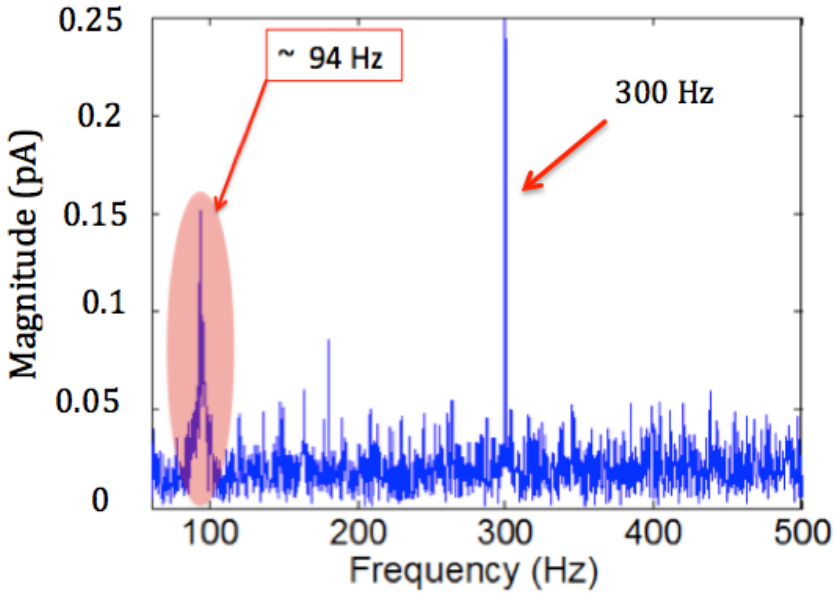

Figure 3.17. The fast Fourier transform (FFT) of (a) the hair velocity measurement due to a mechanical excitation and (b) the corresponding current measurement of the sensor with a 31.75 mm long hair.

The substrate/chamber can also be represented as the structural element that forms the base of the artificial sensor. In doing so, the measured current across the bilayer can be explained as the sensor's response due to a base excitation in a fluid environment. Although the artificial sensor is responsive to a base excitation, frequency analyses demonstrate that both the fluid and mechanical excitation of the artificial hair cell sensor result in a lack of hair vibration being transmitted to the bilayer. This lack of correlation between the hair vibration and the measured current led to the next step of improving the mechanoelectrial transduction between the hair and the picoamp-level current measured across the lipid bilayer.

In an effort to improve this mechanoeletrical transduction, the mechanical coupling between the artificial hair and the structural base of the artificial hair cell is investigated. The goal in fabricating an artificial hair cell system with strong coupling is to create an aquatic sensor with improved correlation between its structural frequency and the

frequency content in its sensing response. Specifically, we investigate the physical properties of the artificial hair and the substrate, a coupled system.

As shown in the frequency analysis of the mechanical excitation measurements (Figure 3.17), the FFT of the hair velocity shows a dominant peak at estimated first natural frequency of the hair (216 Hz), and two frequency peaks associated with the structural base of the hair cell (~ 90 Hz and ~ 120 Hz), but the FFT of the measured current across the bilayer only shows the more dominant frequency peak around 94 Hz. These results demonstrate that the base excitation causes the hair to vibrate and although the vibrations due to hair oscillations are significant, they are not correlated to the measured current across the bilayer. Instead, the vibration of the structural base due to the mechanical excitation is responsible for the sensor's response. This lack of vibration transmission is due to the great disparity between the mass of the hair and the mass of the substrate. In other words, the vibrations of the greater mass (sensor base) are transmitted to the smaller mass (hair), while the vibrations of the smaller mass (hair) are not transferred to the larger mass (sensor base). Therefore, our next step in the sensor fabrication was to strengthen the coupling of the hair and the structural base. Specifically, by matching the first natural frequency of the hair to the 82 Hz frequency of the structural base, our goal was to increase the amplitude of vibration in our sensor. In order to lower the first natural frequency of the artificial hair, the length of the hair is increased from ~31.75 mm to ~ 50.8 mm. The longer hair now has an approximate natural frequency of 85 Hz, which is a close match to the structural base frequency of 90 Hz.

The effect of this altered mechanical coupling in the sensor is tested through a flow-impulse test, in the same manner as the artificial hair cell with the shorter hair (~31.75 mm). As explained earlier, the effect of fluid excitation on the sensing response is understood by simultaneously measuring the current across the bilayer and tracking the hair's velocity by focusing the laser on the tip of the artificial hair. Unlike the 31.75 mm artificial hair in previous tests, approximately 40% of the longer 50.8 mm (~ 20.32 mm)

hair protrudes from the water surface. This was due to the height limitation of the flow chamber. Figure 3.18 shows two traces: the top plot is the temporal response for the measured velocity of the artificial hair as a pulse-like flow traveled over its surface while the bottom plot is the corresponding temporal response for the measured current across the bilayer. As shown in Figure 3.18 (a), the hair is initially stationary, shown by the small changes in velocity around zero. However, when a pulse of water travels over the hair ($t \approx 0.3\ s$), it vibrates the hair and we see distinct oscillatory changes in the velocity (maximum increase of ~ 20 mm/s) of the hair, but with no dc change. This maximum velocity of approximately 20 mm/s is ~ 10 times higher than the velocity of the shorter hair used in the previous sensor. This drastic increase in velocity is due to the lack of resistance around the top 40% of the hair sticking out of the water. At approximate $t = 0.7\ s$, when there is no flow over the sensor, the measured hair velocity returns to its initial value of approximately zero. The corresponding current measurement across the bilayer shown in Figure 3.18 (b) shows the background current is about 25 pA, but in the presence of a pulse-like flow across the artificial hair cell ($t \approx 0.2\ s$), there is an increase in the amplitude of the current (maximum increase of ~ 10 pA) with no average change in the value. At $t \approx 0.5\ s$, when no flow-induced vibrations are transmitted to the bilayer, the measured current returns to its initial value of approximately 25 pA.

(a)

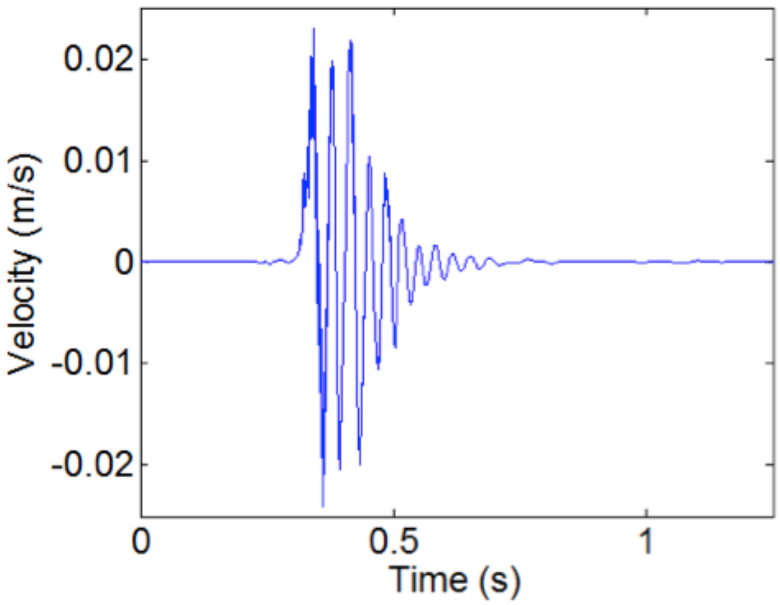

(b)

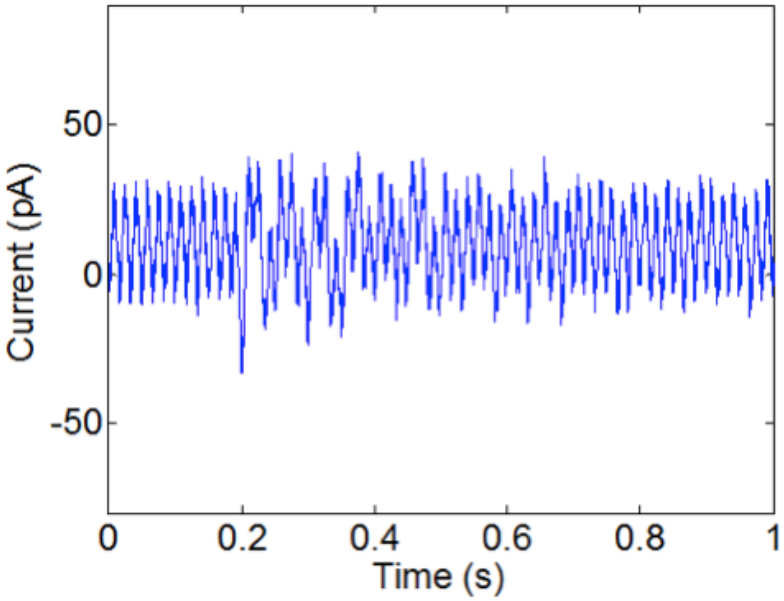

Figure 3.18. (a) The measured hair velocity during flow over the artificial hair cell sensor and (b) the corresponding current response measured across the artificial cell membrane with a 50.8 mm long hair

The time domain response of the hair vibration and bilayer current are both converted into the frequency domain using a fast Fourier transform (FFT). Figure 3.19 shows the two FFT traces: the top plot is the FFT for the measured velocity of the artificial hair as

a pulse-like flow traveled over the sensor's surface while the bottom plot is the corresponding FFT for the measured current across the artificial cell membrane. The frequency analysis of the hair velocity measurement shows some frequency content around the first natural frequency of the hair. Specifically, two distinct peaks are seen around 78 Hz and 95 Hz. Although frequencies near the hair's natural frequency are seen, the most significant frequency peak of ~ 325 Hz significantly varies from the calculated natural frequency of the artificial hair. The absence of a dominant frequency at the first natural frequency of the hair is most likely due to the significant amount of hair sticking out of the water and the lack of force (from the flow) applied at the tip of the hair. Therefore, this dominant frequency could be attributed to the added mass at the bottom half of the artificial hair (as a result of the surrounding fluid) or due to the combination of this added mass and fore application at the midpoint of the hair. On the other hand, the FFT for the measured bilayer current varies from previous results, because there seems to be an increased correlation with the frequency analysis of the laser vibrometer measurements of the artificial hair (Figure 3.19 a). As shown in Figure 3.19 (b), the FFT of the measured current response contains two (although not noticeably significant) frequency peaks at ~ 112 Hz and ~ 129 Hz. These two frequencies seem to correspond to the two hair velocity frequencies at ~ 78 Hz and ~ 95 Hz (Figure 3.19 a) due to their similar double-peak pattern and equal spacing (~17 Hz). Although further investigation is needed to understand the correlation, these results demonstrate that by changing the properties of the hair, the sensor's response is altered. One possible explanation to this shift in frequencies is that the transmission of hair vibrations is affected by the coupling factor introduced by the polyurethane sensor base. Specifically, the polyurethane substrate might be damping out the vibration of the hair.

(a)

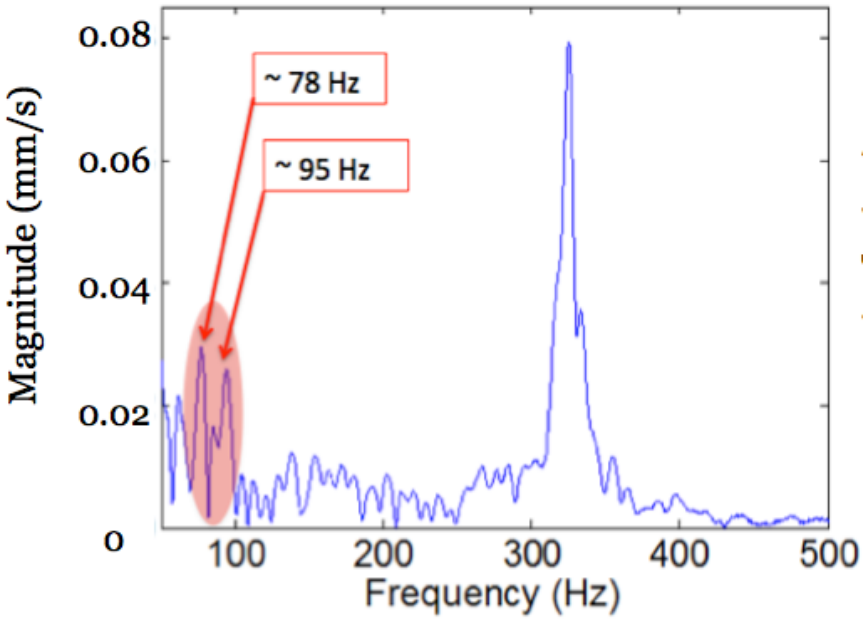

(b)

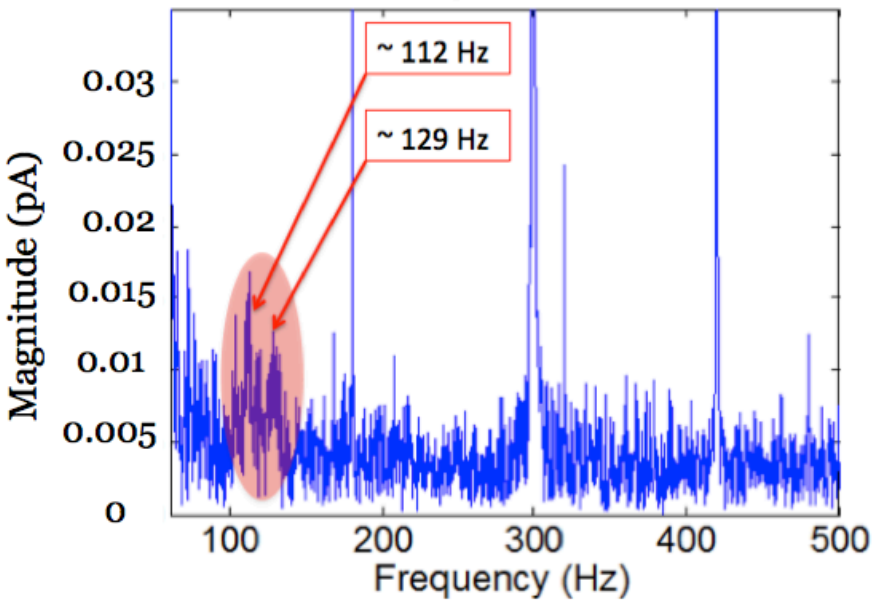

Figure 3.19. The fast Fourier transform (FFT) of (a) the flow-induced hair velocity measurement and (b) the corresponding flow-induced current measurement of the sensor with a 50.8 mm long hair.

The frequency analysis helps to demonstrate that by changing the natural frequency of the hair, the response of the sensor is affected. This change in the sensing response helps to show that the encapsulated artificial hair cell flow sensor is capable of sensing changes in flow through a mechanoelectrical response that is dependent on the vibrations of its embedded artificial hair.

3.3 Summary and Conclusions

In this study, an encapsulated membrane-based hair cell flow sensor was fabricated and tested. Specifically, the artificial aquatic flow sensor was sealed using a low-density polyurethane 'skin' and shown to effectively allow for stable bilayer formation when submerged in an aqueous environment. Initially, two sensor configurations were tested in a flow chamber in order to gain an understanding of the encapsulated system's sensing capabilities: an encapsulated sensor with and without an artificial hair. The artificial hair used in this hair cell was ~ 25.4 mm in length. Flow-induced current measurements of the membrane-based artificial hair cell showed that the presence of a hair resulted in an oscillatory current response with a lower frequency and a longer dissipation time when compared to the sensor lacking an artificial hair. These initial studies helped show that the sensor's flow sensing response was a function of the sensor's surface morphology, however no studies were carried out in order to investigate the correlations between the hair vibration and the measured current.

The next group of experiments was therefore carried out in order to better understand the sensor's response and dynamics as a function of its surface morphology and structural properties. Specifically, the correlation between the motion of the hair and the measured current response was studied through synchronized motion tracking of the hair with a laser vibrometer and current measurements across the bilayer. In the first set of experiments, the response of an artificial hair cell with a 31.75 mm hair was studied. Simultaneous velocity and current measurements proved that the flow over the

sensor affects both the velocity of the hair and the current across the bilayer, however frequency analyses of the measurements demonstrated that the changes in current are not due to the vibrations of the hair, but instead to vibration of the substrate. Since the substrate vibration seemed to play a significant role in the measured current, the next step was to better understand the mechanical coupling between the sensor's substrate and artificial hair. This was done through mechanical excitation of the sensor's base. Frequency analysis of both the hair velocity and measured current proved that current across the bilayer during a mechanical excitation is not correlated to the motion of the hair, but instead to the vibration of the sensor's base. Although the artificial sensor is responsive to an excitation of the base, the studies carried out demonstrated that both the fluid and mechanical excitation of the artificial hair cell result in a lack of hair vibration being transmitted to the bilayer.

This inability of the hair vibrations to be transmitted to the bilayer is due to the great disparity between the mass of the hair and the mass of the substrate. Therefore, our next step was to improve the mechanoelectrial transduction between the hair and the generated current across the artificial cell membrane through stronger mechanical coupling. This was done by matching the first natural frequency of the hair to the frequency of the structural base and in the hope of increasing the amplitude of vibration in our sensor. Specifically, the natural frequency of the artificial hair was altered by increasing the length of the hair to ~ 50.8 mm. The effect of this newly designed artificial hair sensor with a longer hair on its sensing response was tested through fluid excitation over the surface of the sensor. As done in previous tests, frequency investigations suggested an increased correlation between the vibration of the hair and the measured current across the bilayer. A similar double-peak pattern with equal spacing (~17 Hz) was seen in both FFTs. Although a shift in frequencies was apparent, this is likely due to the fact that the transmission of hair vibrations is affected by the coupling factor introduced by the polyurethane sensor base. Although future work needs to be done, these preliminary studies demonstrate that the 'skin'-encapsulated artificial hair cell flow sensor is capable of sensing changes in flow through a

mechanoelectrical response that is dependent on the vibrations of its embedded artificial hair.

Chapter 4

Conclusions and Future Work

4.1 Project Conclusions

4.1.1 Fabrication and Characterization of Carbon-based flow sensor

In this work, carbon nanomaterial/PDMS film sensors (SWCNT/PDMS and SWCNH/PDMS) are fabricated based on techniques developed in previous studies. Although our sensors have considerable levels of surface coverage, microscopy and electrical resistance measurements of the finished samples showed that the surface film is not purely comprised of CNT or CNH material, but of the insulating PDMS layer. An understanding of the electrical impedance of the sensor in water was achieved through EIS measurements of the submerged electroded sensors. These measurements demonstrated that the conduction between the electrodes occurs both across the resistive composite carbon film and through the conductive electrolyte. During flow tests, the voltage measurements across the two electrodes showed varying responses of SWCNT/PDMS sensors. This inconsistency in the flow-induced voltage is attributed to the fabrication method, which can result in insufficient exposure of carbon material on the surface of our PDMS substrate.

The next set of experiments involved using oxygen plasma to improve the sensing capability of the sensors by increasing the interaction between the carbon nanomaterial/PDMS film and the electrolyte fluid through. Plasma treatment of the

carbon-based sensors was conducted in order to render the PDMS on the surface hydrophilic. The increased attraction of water towards the carbon material on the sensor's surface was verified through improvement in the measured flow-induced voltage of the sensors. An average increase in voltage of approximately 20 mV with saturation at the higher flow velocities was seen by SWCNT/PDMS film. On the other hand, the SWCNH/PDMS films, which likely have an insufficient amount of exposed carbon nanohorns, showed distinct increases (compared to pre-plasma treatment) in the measured voltage and generated flow-induced voltages of 1.5-2.25 mV. Overall, the sensitivity of the both classes of sensors was shown to improve after plasma treatment.

4.1.2 Flow Sensor Using an Artificial Cell Membrane

In this study, a 'skin'- encapsulated membrane-based hair cell flow sensor is fabricated and studied. Specifically, a low-density polyurethane 'skin' is used to seal the sensor and is shown to effectively allow for stable bilayer formation when submerged in an aqueous environment. In order to initially characterize the sensor, flow-induced current measurements of the bio-inspired sensor are carried out with and without an embedded hair (~25.4 mm). The measurements showed that the presence of a hair resulted in an oscillatory current response with a lower frequency and a longer dissipation time when compared to the sensor lacking an artificial hair. Therefore, these preliminary results helped show that the sensor's flow sensing response was a function of the sensor's surface morphology.

The next group of studies was conducted in order to investigate the correlations between the hair vibration and the measured current. Through initial synchronized motion tracking of the hair (~ 31.75 mm) with a laser vibrometer and current measurements across the bilayer as function of fluid and mechanical excitation, it is demonstrated that the sensing response of the artificial hair cell lacks the transmission of hair vibrations to the bilayer. Therefore, in an effort to strengthen the coupling

between the hair and substrate, the hair's length is increased to ~ 50.7 mm in order to match the first natural frequency of the hair to the frequency of the sensor's base. The effect of this on the sensor's response was evident in the frequency analysis comparison between the current measured across the bilayer and the hair velocity during fluid excitation of the artificial hair cell. Specifically, the frequency analysis showed a correlation between the frequencies of the hair vibration and the measured current. Although there appeared to be a coupling factor involved between the hair vibration and the current (due to shifted frequencies), these results demonstrate the capability of the bio-inspired sensor to detect changes in flow through a mechanoelectrical response that is dependent on the vibrations of its artificial hair.

4.2 Future Plans

4.2.1 Carbon-based Flow Sensor

Our future efforts in this work should be to develop a better understanding of how surface structuring of the carbon nanomaterial affects both the electrical impedance of the material and the sensor response. Through SEM, XPS, and AFM measurements of the composite film, we should aim to refine our fabrication methods for producing more conductive and hydrophilic films that increase the interaction between the carbon nanomaterial and the water phase. One consideration for improving this interaction between the carbon nanomaterial and the fluid is to develop a more consistent fabrication method that guarantees good surface coverage of the carbon material. A possible future fabrication method could be to use partially cured PDMS as the base for embedding carbon nanomaterials. In addition to improving fabrication techniques, the effect of aligned carbon nanotubes (on the PDMS surface) on the measured flow-induced voltage should be examined. In conjunction with improving the fabrication methods of these sensors in order to improve the interaction of the carbon material with the aqueous solution, more efficient and effective methods of electrode attachment and

encapsulation should be investigated. Finally, the effect of a range of flow velocities and flow types will need to be studied with the goal of gaining a better understanding of the flow sensing capability of these carbon nanomaterial sensors. In this fashion, the transduction mechanism of CNTs and CNHs can then be compared to other carbon materials such as carbon peapods, and even graphene.

4.2.2 Flow Sensor Using an Artificial Cell Membrane

In order to better mimic hair cells in nature, a goal for future work can be to scale down the overall dimensions of the artificial hair cell sensor. Specifically, in order to reduce the size (length and diameter of hair and substrate dimensions) of the sensor, microeletromechanical systems (MEMS) fabrication techniques will need to be employed. In doing so, the future development of artificial hair cell arrays will be made convenient and inexpensive.

The low density 'skin' created in this work was shown to effectively encapsulate and waterproof the artificial hair cell. However, in order to use this encapsulation method, the 'skin' needed to be cured as a cap and then placed on top of the sensor. This was done since the uncured 'skin' was partially immiscible with the oil, which resulted in the small volume of oil in the compartments to be absorbed. Since the work presented in this document did not involve testing arrays of artificial hair cells, pouring uncured 'skin' on top of the substrate to seal it was not necessary. Since future work will involve fabrication of arrays, tackling this setback is important. This absorption issue can be solved by either redesigning the substrate to hold a larger volume of oil (the little oil that will be absorbed will not significantly affect bilayer formation) or by altering the properties of the low-density 'skin'. For instance, using a 'skin' that is not immiscible with the oil phase or a 'skin' that can be quickly cured after poured through methods such as UV, would allow for the sensor to be encapsulated by pouring a 'skin' on top.

A significant improvement to the experiments presented in this document would be to deliver a known input to the sensor. The gravity-induced flow tests conducted in this work were kept consistent through constant reservoir heights and water levels, but future testing of the artificial hair cell sensor should use a setup with a known and more controlled flow. This would allow for better understanding of the correlation between the sensor's response and the flow-induced excitation. Furthermore, the experimental setup should be altered so that the delivered flow will not excite the sensor substrate, but instead only the artificial hair. This would eliminate any unnecessary vibrations of the polyurethane substrate. Finally, in the same regard, future work should focus on optimizing the mechanical coupling between the hair and substrate. In addition to varying the properties of the artificial hair (as presented in this work), by simply changing the 2:1 ratio of Part A (hardener) and Part B (urethane elastomer) of the polyurethane substrate, varying substrate properties can be achieved. In doing so, a study can be carried out that optimizes the mechanical coupling between the hair and the substrate in order to maximize the transmission of hair vibrations to the bilayer.

References

[1] J. M. Benyus, *Biomimicry: Innovation Inspired by Nature*. New York, NY: HarperCollins Publishers Inc., 2002.

[2] K. Hargroves, "Innovation inspired by nature: Biomimicry," *Ecos,* vol. 2006, p. 27, 2006.

[3] T. Ifukube, "Artificial organs: recent progress in artificial hearing and vision," *Journal of Artificial Organs,* vol. 12, pp. 8-10, 2009.

[4] S. Mandal, "A Bio-Inspired Active Radio-Frequency Silicon Cochlea," *IEEE journal of solid-state circuits,* vol. 44, pp. 1814-1828, 2009.

[5] H. Shintaku, "Development of piezoelectric acoustic sensor with frequency selectivity for artificial cochlea," *Sensors and actuators. A. Physical.,* vol. 158, p. 183, 2010.

[6] D. J. Lipomi, "Skin-like pressure and strain sensors based on transparent elastic films of carbon nanotubes," *Nature nanotechnology,* vol. 6, pp. 788-792, 2011.

[7] L. King, *Experience Psychology*. New York, NY: McGraw Hill, 2009.

[8] U. Müller, "Cadherins and mechanotransduction by hair cells," *Current opinion in cell biology,* vol. 20, pp. 557-566, 2008.

[9] P. Herring, *The Biology of the Deep Ocean*. New York: Oxford University Press, 2002.

[10] M. A. R. Koehl and J. R. Strickler, "Copepod Feeding Currents: Food Capture at Low Reynolds Number," *Limnology and Oceanography,* vol. 26, pp. 1062-1073, 1981.

[11] J. C. Andrews, "Deformation of the Active Space in the Low Reynolds Number Feeding Current of Calanoid Copepods," *Canadian Journal of Fisheries and Aquatic Sciences,* vol. 40, pp. 1293-1302, 1983/08/01 1983.

[12] G. Dehnhardt, "Seal whiskers detect water movements," *Nature (London),* vol. 394, pp. 235-236, 1998.

[13] T. J. Härkönen, "Food-habitat relationship of harbour seals and black cormorants in Skagerrak and Kattegat," *Journal of zoology (1987),* vol. 214, pp. 673-681, 1988.

[14] C. Phelan, "A biorobotic model of the sunfish pectoral fin for investigations of fin sensorimotor control," *Bioinspiration & biomimetics,* vol. 5, p. 035003, 2010.

[15] H. Bleckmann, "Neurobiology: hydrodynamic stimuli and the fish lateral line," *Nature (London),* vol. 408, pp. 51-52, 2000.

[16] J. C. Liao, "Fish Exploiting Vortices Decrease Muscle Activity," *Science (New York, N.Y.),* vol. 302, pp. 1566-1569, 2003.

[17] Z. Fan, "Design and fabrication of artificial lateral line flow sensors," *Journal of micromechanics and microengineering,* vol. 12, pp. 655-661, 2002.

[18] Y. Yang, "Artificial lateral line with biomimetic neuromasts to emulate fish sensing," *Bioinspiration & biomimetics,* vol. 5, p. 016001, 2010.

[19] A. E. Perry and P. A. Libby, "Hot-Wire Anemometry," *Journal of Applied Mechanics,* vol. 50, pp. 237-238, 1983.

[20] J. Chen, "Artificial Lateral Line And Hydrodynamic Object Tracking," ed: IEEE, 2006, pp. 694-697.

[21] Y. Yang, "Distant touch hydrodynamic imaging with an artificial lateral line," *PNAS : Proceedings of the National Academy of Sciences,* vol. 103, pp. 18891-18895, 2006.
[22] R. Fukang Jiang, "Theoretical and experimental studies of micromachined hot-wire anemometers," ed: IEEE, 1994, pp. 139-142.
[23] J. J. v. Baar, "Micromachined structures for thermal measurements of fluid and flow parameters," *Journal of micromechanics and microengineering,* vol. 11, pp. 311-318, 2001.
[24] T. Ebefors, "Three dimensional silicon triple-hot-wire anemometer based on polyimide joints," ed: Institute of Electrical and Electronics Engineers, 1998, pp. 93-98.
[25] A. J. van der Wiel, "A liquid velocity sensor based on the hot-wire principle," *Sensors and actuators. A. Physical.,* vol. 37-38, pp. 693-697, 1993.
[26] J. M. Engel, J. Chen, L. Chang, and D. Bullen, "Polyurethane rubber all-polymer artificial hair cell sensor," *Microelectromechanical Systems, Journal of,* vol. 15, pp. 729-736, 2006.
[27] J. Chen, J. Engel, and L. Chang, "Development of polymer-based artificial haircell using surface micromachining and 3D assembly," in *TRANSDUCERS, Solid-State Sensors, Actuators and Microsystems, 12th International Conference on, 2003*, 2003, pp. 1035-1038 vol.2.
[28] Y. Ozaki, T. Ohyama, T. Yasuda, and I. Shimoyama, "An air flow sensor modeled on wind receptor hairs of insects," in *Micro Electro Mechanical Systems, 2000. MEMS 2000. The Thirteenth Annual International Conference on*, 2000, pp. 531-536.
[29] J. Van Baar, "Arrays of cricket-inspired sensory hairs with capacitive motion detection," ed: IEEE, 2005, pp. 646-649.
[30] C. Nannan Chen, "Design and Characterization of Artificial Haircell Sensor for Flow Sensing With Ultrahigh Velocity and Angular Sensitivity," *Journal of microelectromechanical systems,* vol. 16, pp. 999-1014, 2007.
[31] M. E. McConney, "Biologically inspired design of hydrogel-capped hair sensors for enhanced underwater flow detection," *Soft matter,* vol. 5, p. 292, 2009.
[32] S. Peleshanko, "Hydrogel-Encapsulated Microfabricated Haircells Mimicking Fish Cupula Neuromast," *Advanced materials (Weinheim),* vol. 19, pp. 2903-2909, 2007.
[33] H. Hu, "Design of 3D Swim Patterns for Autonomous Robotic Fish," ed: IEEE, 2006, pp. 2406-2411.
[34] G. V. Lauder, "Morphology and Experimental Hydrodynamics of Fish Fin Control Surfaces," *IEEE journal of oceanic engineering,* vol. 29, pp. 556-571, 2004.
[35] G. V. Lauder, "Learning from fish: Kinematics and experimental hydrodynamics for roboticists," *International journal of automation and computing,* vol. 3, pp. 325-335, 2006.
[36] G. V. Lauder, "Fish biorobotics: kinematics and hydrodynamics of self-propulsion," *Journal of experimental biology,* vol. 210, pp. 2767-2780, 2007.
[37] M. K. Philen, "Fibrillar Network Adaptive Structure with Ion-transport Actuation," *Journal of intelligent material systems and structures,* vol. 18, pp. 323-334, 2006.
[38] L. Sherwood, *Human Physiology: From Cells to Systems* vol. 7e. Belmont, CA: Brooks/Cole, 2010.
[39] D. J. Hornbaker, "Mapping the One-Dimensional Electronic States of Nanotube Peapod Structures," *Science (New York, N.Y.),* vol. 295, pp. 828-831, 2002.

[40] A. K. Geim, "The rise of graphene," *Nature materials,* vol. 6, pp. 183-191, 2007.
[41] J. Zhang, "In Vitro and in Vivo Studies of Single-Walled Carbon Nanohorns with Encapsulated Metallofullerenes and Exohedrally Functionalized Quantum Dots," *Nano letters,* vol. 10, pp. 2843-2848, 2010.
[42] S. A. Sarles, "Incorporation and characterization of biological molecules in droplet-interface bilayer networks for novel active systems " *International Society for Optics and Photonics,* vol. 7288, 2009.
[43] S. A. Sarles, "Regulated Attachment Method for Reconstituting Lipid Bilayers of Prescribed Size within Flexible Substrates," *Analytical chemistry (Washington),* vol. 82, pp. 959-966, 2010.
[44] S. A. Sarles, "Bilayer Formation between Lipid-Encased Hydrogels Contained in Solid Substrates," *ACS applied materials & interfaces,* vol. 2, pp. 3654-3663, 2010.
[45] H. T. Tien, "The lipid bilayer concept and its experimental realization: from soap bubbles, kitchen sink, to bilayer lipid membranes," *Journal of membrane science,* vol. 189, pp. 83-117, 2001.
[46] J. S. H. Stephen R. Bolsover, Elizabeth A. Shephard, Hugh A. White, and Claudia G. Wiedemann, *Cell Biology: A Short Course* vol. 2nd edition. Hoboken, NJ: John Wiley & Sons, Inc., 2004.
[47] C. Tanford, "The hydrophobic effect and the organization of living matter," *Science (New York, N.Y.),* vol. 200, pp. 1012-1018, 1978.
[48] C. Tanford, *The Hydrophobic Effect: Formation of Micelles and Biological Membranes* vol. 2 edition. New York, NY: John Wiley & Sons, Inc., 1980.
[49] S. J. S. a. G. L. Nicolson, "The fluid mosaic model of the structure of cell membranes," *Science,* 1972.
[50] P. Booth, "Sane in the membrane: designing systems to modulate membrane proteins," *Current opinion in structural biology,* vol. 15, pp. 435-440, 2005.
[51] T. J. McIntosh, "ROLES OF BILAYER MATERIAL PROPERTIES IN FUNCTION AND DISTRIBUTION OF MEMBRANE PROTEINS," *Annual review of biophysics and biomolecular structure,* vol. 35, pp. 177-198, 2006.
[52] (2 June 2012). *Lipid Bilayer*. Available: http://en.wikipedia.org/wiki/Lipid_bilayer
[53] S. A. Sarles, "Membrane-based biomolecular smart materials," *Smart materials and structures,* vol. 20, p. 094018, 2011.
[54] S. A. Sarles, "Hair cell inspired mechanotransduction with a gel-supported, artificial lipid membrane," *Soft matter,* vol. 7, p. 4644, 2011.
[55] S. Ghosh, "Carbon Nanotube Flow Sensors," *Science (New York, N.Y.),* vol. 299, pp. 1042-1044, 2003.
[56] H. Cao, "Fabrication and characterization of patterned carbon nanotube flow sensor cell," *Chinese science bulletin,* vol. 55, pp. 2579-2583, 2010.
[57] S. Ghosh, "Flow-induced voltage and current generation in carbon nanotubes," *Physical review. B, Condensed matter and materials physics,* vol. 70, p. 205423, 2004.
[58] H. Cao, "Single-walled carbon nanotube network/poly composite thin film for flow sensor," *Microsystem technologies : sensors, actuators, systems integration,* vol. 16, pp. 955-959, 2010.
[59] D. Kasuya, "Selective Production of Single-Wall Carbon Nanohorn Aggregates and Their Formation Mechanism," *The journal of physical chemistry. B,* vol. 106, pp. 4947-4951, 2002.

[60] K. Murata, "Pore structure of single-wall carbon nanohorn aggregates," *Chemical physics letters,* vol. 331, pp. 14-20, 2000.
[61] B. H. Jo, "Three-dimensional micro-channel fabrication in polydimethylsiloxane (PDMS) elastomer," *Journal of microelectromechanical systems,* vol. 9, pp. 76-81, 2000.
[62] D. T. Eddington, J. P. Puccinelli, and D. J. Beebe, "Thermal aging and reduced hydrophobic recovery of polydimethylsiloxane," *Sensors and Actuators B: Chemical,* vol. 114, pp. 170-172, 2006.
[63] K. C. Tang, "Evaluation of bonding between oxygen plasma treated polydimethyl siloxane and passivated silicon," *Journal of physics: Conference Series,* vol. 34, pp. 155-161, 2006.
[64] K. Garrison, "Formation, encapsulation, and validation of membrane-based artificial hair cell sensors," in *Society for Optics and Photonics*, 2012.
[65] D. Needham, "Tensions and free energies of formation of," *Biophysical journal,* vol. 41, p. 251, 1983.
[66] M. A. Holden, D. Needham, and H. Bayley, "Functional Bionetworks from Nanoliter Water Droplets," *Journal of the American Chemical Society,* vol. 129, pp. 8650-8655, 2007/07/01 2007.
[67] T. Baba, Y. Toshima, H. Minamikawa, M. Hato, K. Suzuki, and N. Kamo, "Formation and characterization of planar lipid bilayer membranes from synthetic phytanyl-chained glycolipids," *Biochimica et Biophysica Acta (BBA) - Biomembranes,* vol. 1421, pp. 91-102, 1999.
[68] D. J. Inman, *Engineering Vibration, 2nd ed.* Upper Saddle River, New Jersey: Prentice-Hall, 2001.